AFRL-RW-EG-TR-2013-031

Preliminary Study of Turbulence for a Lobed Body in Hypersonic Flight

Douglas V. Nance

AFRL/RWWC
STE 334
101 W. Eglin Blvd.
Eglin AFB, FL 32542-6810

February 2013

FINAL REPORT

AIR FORCE RESEARCH LABORATORY
MUNITIONS DIRECTORATE

■ **Air Force Materiel Command** ■ **United States Air Force** ■ **Eglin Air Force Base, FL 32542**

NOTICE AND SIGNATURE PAGE

Using Government drawings, specifications, or other data included in this document for any purpose other than Government procurement does not in any obligate the U.S. Government. The fact that the Government formulated or supplied the drawings, specifications, or other data does not license the holder or any other person or corporation, or convey any rights or permission to manufacture, use, or sell any patented invention that may relate to them.

This report was cleared for public release by the 96th Air Base Wing, Public Affairs Office, and is available to the general public, including foreign nationals. Copies may be obtained from the Defense Technical Information Center (DTIC) < http://www.dtic.mil/dtic/index/html>.

AFRL-RW-EG-TR-2013-031 HAS BEEN REVIEWED AND IS APPROVED FOR PUBLICATION IN ACCORDANCE WITH ASSIGNED DISTRIBUTION STATEMENT.

FOR THE DIRECTOR:

Signed	Signed
Craig R. Ewing, DR-IV, PhD	Douglas V. Nance
Technical Advisor	Research Scientist
Weapon Engagement Division	AFRL/RWWC

This report is published in the interest of scientific and technical information exchange, and its publication does not constitute the Government's approval or disapproval of its ideas or findings.

REPORT DOCUMENTATION PAGE

Form Approved
OMB No. 0704-0188

PLEASE DO NOT RETURN YOUR FORM TO THE ABOVE ADDRESS.

1. REPORT DATE *(DD-MM-YYYY)*	2. REPORT TYPE	3. DATES COVERED *(From - To)*
22-02-2013	Final	Oct 2011 - Sep 2012

4. TITLE AND SUBTITLE

Preliminary Study of Turbulence for a Lobed Body in Hypersonic Flight

5a. CONTRACT NUMBER

N/A

5b. GRANT NUMBER

N/A

5c. PROGRAM ELEMENT NUMBER

61102F

6. AUTHOR(S)

Douglas V. Nance

5d. PROJECT NUMBER

3002

5e. TASK NUMBER

FW

5f. WORK UNIT NUMBER

28

7. PERFORMING ORGANIZATION NAME(S) AND ADDRESS(ES)

AFRL/RWWC
STE 334
101 W. Eglin Blvd.
Eglin AFB, FL 32542-6810

8. PERFORMING ORGANIZATION REPORT NUMBER

AFRL-RW-EG-TR-2013-031

9. SPONSORING/MONITORING AGENCY NAME(S) AND ADDRESS(ES)

Air Force Office of Scientific Research
875 N. Randolph Street
Arlington, VA 22203

10. SPONSOR/MONITOR'S ACRONYM(S)

AFRL-RW-EG-TR

11. SPONSOR/MONITOR'S REPORT NUMBER(S)

AFRL-RW-EG-TR-2013-031

12. DISTRIBUTION/AVAILABILITY STATEMENT

Distribution A. Approved for public release, distribution unlimited. (96ABW-2013-0024)

13. SUPPLEMENTARY NOTES

14. ABSTRACT

The present study addresses the aerodynamics of a lobed body immersed in a Mach 6 hypersonic flow field at sea level. As a first study of this type, the shape of the body is held fixed, and the flow field is resolved by applying state-of-the-art large eddy simulation techniques in conjunction with a hybrid shock-turbulence capturing algorithm. Air is treated as a mixture of nitrogen and oxygen, and the governing equations are closed by a modern compressible turbulence closure term. Pressure is determined by using the thermally perfect gas equation of state applied to each species. The distribution of temperature is determined on the body surface as well as temperature gradients based upon adiabatic wall boundary conditions. The structure of the flow field is examined as is the time required for stationarity. Both turbulent statistics and spectra are determined at points on the surface of the body. Times series analyses are performed for aerodynamics forces encountered by the body.

15. SUBJECT TERMS

LES, turbulence, shock wave, covariance matrix

16. SECURITY CLASSIFICATION OF:			17. LIMITATION OF ABSTRACT	18. NUMBER OF PAGES	19a. NAME OF RESPONSIBLE PERSON
a. REPORT	b. ABSTRACT	c. THIS PAGE			K. J. Vanden
UNCLAS	UNCLAS	UNCLAS	UL	46	19b. TELEPHONE NUMBER *(Include area code)*

Reset

Standard Form 298 (Rev. 8/98)
Prescribed by ANSI Std. Z39.18

Table of Contents

List of Figures

SUMMARY

The present study addresses the aerodynamics of a lobed body immersed in a Mach 6 hypersonic flow field at sea level. As a first study of this type, the shape of the body is held fixed, and the flow field is resolved by applying state-of-the-art large eddy simulation techniques in conjunction with a hybrid shock-turbulence capturing algorithm. Air is treated as a mixture of nitrogen and oxygen, and the governing equations are closed by a modern compressible turbulence closure term. Pressure is determined by using the thermally perfect gas equation of state applied to each species. The distribution of temperature is determined on the body surface as well as temperature gradients based upon adiabatic wall boundary conditions. The structure of the flow field is examined as is the time required for stationarity. Both turbulent statistics and spectra are determined at points on the surface of the body. Times series analyses are performed for aerodynamics forces encountered by the body.

1 INTRODUCTION

The past two decades have been witness to major advances in computing power, particularly in the area of parallel computing. For instance, in 1995, the author's doctoral research was performed on a CRAY Y-MP with vector registers, 512 MB of memory and a clock speed of 167 MHz. The system had no more than eight vector processors and had less capability than the ThinkMate 8-Way system (32 cores) that resides by my desk. Now, we have high performance computers (HPC) platforms such as RAPTOR, a CRAY XE6 with 40,000 cores and 2GB memory per node. There are 32 cores per node making for a staggering improvement in computational capability. This windfall in computer power constitutes a boon for the field of computational physics. Modest improvements in numerical algorithms, particularly those for solving partial differential equations (PDEs), can now be fully implemented and exercised with fewer restrictions imposed by memory size or execution speed. Fields such as Computational Electromagnetics (CEM), Computational Structural Mechanics (CSM) and Computational Fluid Dynamics (CFD) can benefit from the use of research-grade numerical schemes and state-of-the-art material models. In some cases, computational tasks requiring several weeks of computer time (just five years ago) can now be completed in a few hours. We do not exaggerate when today we claim that many chemical dynamics and material modeling problems can be solved via Quantum Chemistry algorithms on HPC systems. Budgetary considerations aside, it is a fortuitous time to work in the field of Computational Physics.

From an egocentric standpoint, the field of CFD is undergoing a transition. Aside from its earlier focus on solving problems in aerodynamics, CFD is now working to incorporate additional physics within its algorithmic bag of tricks. Some of the more recent and important work enables both shock waves and turbulent eddies to be captured without mutual degradation.[1,2] State-of-the-art dynamic methods for Large Eddy Simulation (LES) of turbulence are also carried into the realm of shock physics as a unified algorithm. This advance presents a powerful toolset for capturing the physics of extreme environments such in the violent interior of stars or in the core of manmade explosions.[3,4] The current research field, regarded hereafter as Multiphase Physics (MP), concentrates on simulating matter fields of just level of complexity where multiple phases of matter may be involved along with chemistry and extreme pressures and temperatures. What is extreme? From the standpoint of some of our recent work, extreme may be defined as temperatures above 5000˚K or pressures cast in the Giga-Pascal range. Naturally, MP problems are quite realistic in that they may contain solid particles or liquid droplets that combust or react chemically with a surrounding gaseous, turbulent flow field.[5] From our point of view, a properly formulated set of numerical algorithms contains all of the requisite physics for the problem; these algorithms, in turn, autonomously resolve the problem physics based upon only the input parameters such as geometry and initial conditions (including the relevant chemical species). It is out desire to minimize or even eliminate any processes such as "tuning" of "calibration" of the computer algorithms undertaken on the part of the user. The problem under study below exemplifies this idea.

As we alluded to earlier, the physics of extreme environments is very interesting. The hypersonic flow field created around a solid body under sea level flight conditions is an example of just such an environment. Although hypersonic flow was of great interest in the final quarter

of the twentieth century, the focus of the research was largely confined to high altitude flight. This effort was motivated by the space program. We are concerned with the behavior of hypersonic flow in the thick atmosphere where gases such as oxygen and nitrogen have higher partial pressures. In combination with trace gases, these species are likely to react chemically near the surface of an immersed body. As one may expect, temperatures will soar in the body's boundary layer as viscous forces slow the flow stream to satisfy the no-slip boundary condition. The variation in temperature can vary over a wide range, so our equation of state (EOS) must correctly capture changes in the gaseous specific heats. It is worth noting that the older calorically perfect gas model over predicts temperatures. During the period of time encompassing the 1960s through the 1980s, hypersonic flow and high temperature gas dynamics were intensively studied because of the design needs of reentry vehicles and concept designs such as the National Aerospace Plane.[6] In deference to supersonic flow, there is no strict point of demarcation in terms of speed heralding the hypersonic regime. For aerospace vehicles commonly studied, the onset of hypersonic flow physics is encountered in the range of Mach 3 to Mach 5, or even higher. The physics associated with this regime is very different that that associated with slower speed flow. Hypersonic flow is characterized by the presence of thin shock layers that lie between the body and the shock wave.[6] At higher Mach numbers, this layer becomes even thinner, and it may even merge with the boundary layer. The presence of an entropy layer is also characteristic of many hypersonic bluff body flow fields. Bluff (or blunted) bodies cause the formation of curved shock waves that stand some distance away from the body. The strength of the shock wave and the attendant entropy jump changes along with shock curvature. It is strongest at the "nose" and weakens as the shock wave straightens downstream. This effect causes a flow with strong entropy and vorticity gradients to wash down the body thickening the boundary layer.[6] High temperature gas dynamics are often encountered in hypersonic flow fields. In order to satisfy the no-slip boundary condition, the flow must reduce from hypersonic speed outside of the boundary layer to zero at the body surface. This situation stands in stark contrast to earlier models of hypersonic flow that allow slip (or tangential flow) at the body surface. The mechanism decreasing the flow speed is viscous dissipation or friction. The kinetic energy of the flow is transformed into the internal energy of gas molecules in the boundary layer. As a result, boundary layer temperature increases dramatically.[7] In slower speed flow fields, this energy is absorbed mostly in molecular translational and rotational modes, but for hypersonic speeds, energy may be absorbed in vibrational modes.[8] The existence of the latter mode tends to moderate the rise in temperature and motivates the use of more advanced EOS models for gas mixtures.

Over more complex body shapes, the attendant high Reynolds number leads us to expect the formation of pockets of turbulent flow. It is important that our physics simulation capture this behavior since turbulence has a potent effect over chemical reactions. In turn, chemical reactions affect temperature at the body surface. All of these effects combine to shape the aerodynamic forces (or loads) exerted on the body. The loads, of course, exert a great deal of influence over the body's flight stability. A goal of this report is to investigate the evolution of turbulent flow at hypersonic speeds under sea level flight conditions. It is desirable to consider an immersed body with enough complexity to support turbulent flow while retaining the ease of single block grid generation. As is shown in Figure 1, our test body has a complex shape characterized by a blunt nose and an elongated body distending into fin-shaped lobes. The body is immersed in a Mach 6

flow field with angle of attack and side slip angle both fixed at 5˚. The grid for this body is generated through the use of algebraic techniques; the specifics are discussed later in this report.

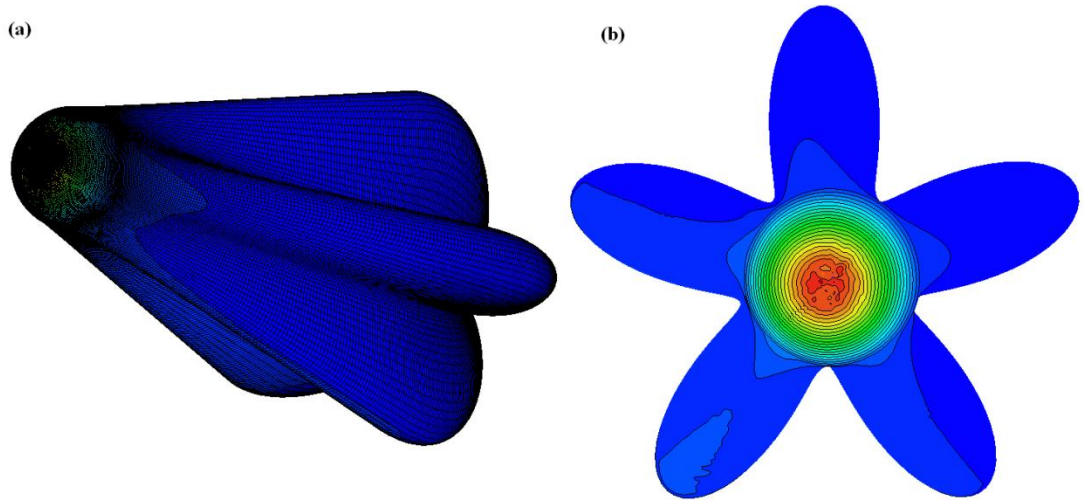

Figure 1. Single-Block Test Geometry

State-of-the-art LES techniques are used to simulate flow around the body at the aforementioned flight conditions. These methods allow the viscous, turbulent flow field to be resolved with high accuracy. Adiabatic wall conditions are enforced at the solid surface for the resolution of temperature. In the course of the simulation, the time required to achieve a stationary flow field is determined. Flow properties vary in a cyclical manner indicative of a stationary flow. Pressure, subgrid kinetic energy, temperature and temperature gradient distributions are also determined on the body surface. Velocity correlations, turbulent kinetic energy spectra and probability distribution functions for fluctuating velocity components are determined at points near the body surface.

The remainder of this report is organized as follows. Section 2 contains an exposition of the theory behind our LES methodology including current research in subgrid models. Section 3 contains brief descriptions of the numerical techniques used in LESLIE3D as well as a discussion of our grid generation technique. The statistical analysis techniques employed are also briefly presented. Some of the specifics associated with the set-up of our simulation are presented in Section 4. Section 5 contains the results of our simulations at Mach 6 along with the analyses produced by statistical post-processing. Section 6 of the report is dedicated toward conclusions along with a wrap-up of our findings.

2 THEORY

The numerical flow field solutions described below have been generated by using the Large Eddy Simulation with LInear Eddy modeling in 3 Dimensions (LESLIE3D) computer program. LESLIE3D is a state-of-the-art MP research tool developed by Suresh Menon at the Georgia

Institute of Technology.[9] This computer program has a core capability for dynamic large eddy simulation (LES). That is to say, flow field features existing at the scale of the grid or larger are simulated by numerical solution of the conservation equations. Flow features existing at the subgrid scales (scales smaller than the mesh size) are modeled.[10] The subgrid effects are represented in the conservation equations via closure terms. The theory behind LESLIE3D is described in the following sections.

2.1 Filtered Governing Equations

The gas phase conservation laws used in LESLIE3D consist of the compressible Navier-Stokes equations cast in three dimensions. For real turbulent flow fields (in spite of today's computer resources), we cannot solve these equations via direct numerical simulation (DNS) for Reynolds numbers exceeding 8000.[11] One may recall that hypersonic flow fields are characterized by Reynolds number of one million or more. Our LES approach first involves spatially filtering the governing equations at the grid scale in order to produce a set of turbulence closure terms that are later modeled.[12] The Navier-Stokes equations are filtered in order to permit the large spatially dependent scales for fluid motion to be separated from the small universal scales.[13] In the equations below, the overbar indicates a spatially filtered quantity while the tilde (~) indicates a mass averaged property, i.e.,

$$\tilde{f} = \frac{\overline{\rho f}}{\bar{\rho}} \tag{1}$$

The filtered Navier-Stokes equations may be written

$$\frac{\partial \bar{\rho}}{\partial t} + \frac{\partial \bar{\rho}\tilde{u}_i}{\partial x_i} = 0 \tag{2}$$

$$\frac{\partial \bar{\rho}\tilde{u}_i}{\partial t} + \frac{\partial}{\partial x_j}[\,\bar{\rho}\tilde{u}_i\tilde{u}_j + \bar{P}\delta_{ij} - \bar{\tau}_{ij} + \tau_{ij}^{sgs}\,] = 0 \tag{3}$$

$$\frac{\partial \bar{\rho}\tilde{E}}{\partial t} + \frac{\partial}{\partial x_i}[\,(\bar{\rho}\tilde{E} + \bar{P})\,\tilde{u}_i + \bar{q}_i - \tilde{u}_j\bar{\tau}_{ij} + H_i^{sgs} + \sigma_i^{sgs}\,] = 0 \tag{4}$$

$$\frac{\partial \bar{\rho}\tilde{Y}_k}{\partial t} + \frac{\partial}{\partial x_i}[\,\bar{\rho}\tilde{Y}_k(\tilde{u}_i + \tilde{V}_{i,k}) + Y_{i,k}^{sgs} + \theta_{i,k}^{sgs}\,] = \overline{\dot{\omega}}_k \tag{5}$$

where $k = 1,\ldots,N_s$, N_s being the number of gaseous chemical species involved in the calculation. Equations (2) through (5) are mass, momentum, energy and species conservation equations, respectively. Symbols ρ, u_i, P, Y_k and q_i are the mixture gas density, velocity component in Cartesian component direction x_i, absolute pressure, mass fraction for the k^{th} species and heat

flux component in direction x_i, respectively. Symbol τ_{ij} contains the components of the Cartesian shear stress tensor while E represents the total energy per unit volume, i.e.,

$$\tau_{ij} = \mu\left(\frac{\partial u_i}{\partial x_j} + \frac{\partial u_j}{\partial x_i}\right) + \lambda \frac{\partial u_l}{\partial x_l}\delta_{ij} \tag{6}$$

$$E = e + \frac{1}{2}u_l u_l \tag{7}$$

The summation convention is applied to the index l in (6) and (7). The Fickian diffusion velocities are given by $V_{i,k}$. The subgrid stress tensor τ_{ij}^{sgs}, subgrid total enthalpy flux H_i^{sgs}, subgrid convective species flux Y_{ij}^{sgs}, subgrid viscous work σ_i^{sgs} and subgrid species diffusive work $\theta_{i,k}^{sgs}$ are subgrid quantities produced by the filtering process. Their exact forms may be written as

$$\tau_{i,j}^{sgs} = \bar{\rho}(< u_i u_j > - \tilde{u}_i \tilde{u}_j) \tag{8}$$

$$H_i^{sgs} = \bar{\rho}\,(< E\,u_i > - \tilde{E}\,\tilde{u}_i) + \overline{u_j P} - \bar{P}\,\tilde{u}_j \tag{9}$$

$$Y_{ik}^{sgs} = \bar{\rho}(< u_i Y_k > - \tilde{u}_i \tilde{Y}_k) \tag{10}$$

$$\sigma_i^{sgs} = -(\overline{u_j \tau_{ij}} - \tilde{u}_j \bar{\tau}_{ij}) \tag{11}$$

$$\theta_{ik}^{sgs} = \bar{\rho}(< V_{ik} Y_k > - \tilde{V}_{ik} \tilde{Y}_k) \tag{12}$$

The filtered species diffusion velocities are given by

$$\tilde{V}_{ik} = -\frac{D_k}{\tilde{Y}_k}\frac{\partial \tilde{Y}_k}{\partial x_i} \tag{13}$$

where D_k is the diffusion coefficient for species *k*. In equations (8) through (12), the arrowhead brackets "< >" denote mass averaging as does the "~" notation. These equations contain averages of products between variables. The repeated index in (12) does not imply summation. Not being known *a priori*, the subgrid terms must be treated as variables. The result is that the system of filtered governing equations now has more variables than equations and cannot directly be closed for solution. Closure can only be accomplished by modeling these subgrid quantities.[10]

Thermochemical and thermophysical behavior for the system must also be described. Chemical reactions occurring between species are governed by a reaction mechanism specified

by the user. The rate of mass transfer of between species is given by $\overline{\dot{\omega}}_k$, the filtered reaction rate term.[12] Pressure and temperature in the gas mixture are determined through the use of a filtered perfect gas equation of state, i.e.,

$$\overline{P} = \overline{\rho}(\tilde{R}\tilde{T} + T^{sgs}) \tag{14}$$

with R_U equal to the universal gas constant, and

$$\tilde{R} = \sum_{k=1}^{N_s} \tilde{Y}_k R_k = \sum_{k=1}^{N_s} \tilde{Y}_k \left(\frac{R_U}{MW_k} \right) \tag{15}$$

MW_k is the molecular weight of species k . The sum of subgrid species-temperature correlations is given by T^{sgs}, i.e.,

$$T^{sgs} = \sum_{k=1}^{Ns} \frac{< Y_k \, T > - \tilde{Y}_k \, \tilde{T}}{MW_k} \tag{16}$$

The filtered mixture internal energy may be expressed as

$$\tilde{e} = \sum_{k=1}^{N_s} \tilde{Y}_k e_{f,k}^0 + \sum_{k=1}^{N_s} \tilde{Y}_k \int_0^{\tilde{T}} C_{V,k}(T)\, dT + \sum_{k=1}^{N_s} E_k^{sgs} \tag{17}$$

In equation (9), $C_{V,k}$ is the constant volume specific heat for species k , and E_k^{sgs} is the subgrid internal energy for species k , i.e.,

$$E_k^{sgs} = < Y_k \, e_k(T) > - \tilde{Y}_k \, \tilde{e}_k(\tilde{T}) \tag{18}$$

The heat flux term may be written as

$$\overline{q}_i = -\kappa(\tilde{T}) \frac{\partial \tilde{T}}{\partial x_i} + \overline{\rho} \sum_{k=1}^{N_s} \tilde{h}_k(\tilde{T}) \, \tilde{Y}_k \, \tilde{V}_{i,k} + \sum_{k=1}^{Ns} q_{i,k}^{sgs} \tag{19}$$

where κ is the local coefficient of thermal conductivity.[9] The subgrid species heat flux may be expressed (with no summation over k) as

$$q_{ik}^{sgs} = \overline{\rho}(< h_k \, Y_k \, V_{ik} > - \tilde{h}_k \, \tilde{Y}_k \, \tilde{V}_{ik}) \tag{20}$$

Note that repeated indices in (18) and (20) do not imply summation. Also the filtered sensible species enthalpy is

$$\tilde{h}_k = \tilde{Y}_k h_{f,k}^0 + \tilde{Y}_k \int_0^{\tilde{T}} C_{P,k}(T)\, dT \tag{21}$$

The specific heat at constant pressure for species k is written as

$$C_{P,k} = C_{V,k} + R_k \tag{22}$$

2.2 Modeling Correlations to Obtain Closure

The subgrid terms, denoted by superscript "*sgs*" cause difficulties in closing the system of governing equations. LES fixes this problem by modeling these terms based upon the resolved flow properties. Specifically, we neglect T^{sgs}, θ_{ik}^{sgs}, q_{ik}^{sgs} and E_k^{sgs} since these terms tend to be small.[12] The crux of the modeling process lies in the determination of the subgrid stress tensor based upon the subgrid kinetic energy, i.e.,

$$\tau_{ij}^{sgs} = -2\,\bar{\rho}\,\nu_t \left(\tilde{S}_{ij} - \frac{1}{3}\tilde{S}_{kk}\delta_{ij} \right) + \frac{2}{3} k^{sgs} \delta_{ij} \tag{23}$$

where the evolution equation for subgrid kinetic energy is given by

$$\begin{aligned} \frac{\partial}{\partial t}(\bar{\rho} k^{sgs}) + \frac{\partial}{\partial x_i}(\bar{\rho}\tilde{u}_i k^{sgs}) &= \frac{\partial}{\partial x_i}\left[(\bar{\rho}\nu_t + \mu)\frac{\partial k^{sgs}}{\partial x_i} + \frac{\bar{\rho}\nu_t}{\mathrm{Pr}_t}\tilde{R}\frac{\partial \tilde{T}}{\partial x_i} \right] \\ &\quad - \overbrace{\left(1 + \alpha_{pd}(M_t^{sgs})^2 \left(\frac{\bar{\rho}\tilde{S} k^{sgs}}{D_k^{sgs}} \right)^2 \right)}^{*} \left(\tau_{ij}^{sgs}\frac{\partial \tilde{u}_j}{\partial x_i} + \bar{\rho}\mathrm{K}_\varepsilon \frac{(k^{sgs})^{3/2}}{\bar{\Delta}} \right) \end{aligned} \tag{24}$$

The subgrid kinetic energy is mathematically defined as

$$k^{sgs} = \frac{1}{2}(< u_i u_i > - \tilde{u}_l \tilde{u}_l) \tag{25}$$

where the summation convention is in effect for the index l.[9] Equation (24) is integrated along with the conservation equations, and as a model equation, relies on a set of parameters such as the eddy viscosity ν_t given by

$$\nu_t = \mathrm{K}_\nu \sqrt{k^{sgs}}\,\bar{\Delta} \tag{26}$$

where K_ν is a coefficient set by the Locally Dynamic subgrid Kinetic energy Model (LDKM).[9] The dissipation term for k^{sgs} is

$$D_{K^{sgs}} = \frac{\bar{\rho} \mathrm{K}_{\varepsilon} (k^{sgs})^{3/2}}{\bar{\Delta}} \tag{27}$$

with K_{ε} as the LDKM dissipation coefficient (analogous to K_{ε}); $\bar{\Delta}$ is the local grid scale measurement. For most problems, K_{ν} and K_{ε} are set to 0.067 and 0.931, respectively. Other parameters introduced in (24) are μ the dynamic viscosity, Pr_t the turbulent Prandtl number, M_t^{sgs} the turbulent Mach number based upon k^{sgs}, and α_{pd} is a pressure-dilatational scaling coefficient. Note also that (23) and (24) are tightly coupled through the presence of both k^{sgs} and τ_{ij}^{sgs}.

The theory that underlies LDKM is quite complex, and the details of implementing the above equations (along with others not shown) are beyond the scope of this report. This statement is especially true when we employ the algorithms developed for dynamically updating K_{ν} and K_{ε}. Still, it is worthwhile to discuss the motivation behind this model. In the first place, one may take note of the number of coefficients existing in (24), (26) and (27). The proliferation of coefficients indicates that LDKM is indeed a model, but these coefficients are not tunable. Instead, they are in most cases based upon knowledge of the dynamic behavior of turbulent compressible flow fields. That is to say, these coefficients are set either autonomously by LDKM operating in dynamic mode or remain fixed as described above.[12] Also, LDKM diverges from most contemporary dynamic LES models through the presence of the term marked by an (*) asterisk. This term represents dilatational effects within the flow field due to pressure. It is through this term that (24) becomes representative of highly compressible flow fields. This equation stands as an example of state-of-the-art research in this field. When operating LDKM in dynamic mode, the subgrid scale properties are made to behave in an inertially correct manner with respect to the resolved flow field.

The remainder of the subgrid terms are not as difficult to model although the subgrid kinetic energy is still relied upon (at least in part). H_i^{sgs} and σ_i^{sgs} are modeled as one by using eddy viscosity closure form, i.e.,

$$H_i^{sgs} + \sigma_i^{sgs} = -(\bar{\rho}\nu_t + \mu)\frac{\partial k^{sgs}}{\partial x_i} - \frac{\bar{\rho}\nu_t C_p}{\mathrm{Pr}_t}\frac{\partial \tilde{T}}{\partial x_i} + \tilde{u}_j \tau_{ij}^{sgs} \tag{28}$$

The subgrid diffusion of species mass fractions is modeled by using an eddy diffusivity form, i.e.,

$$Y_{ik}^{sgs} = -\frac{\bar{\rho}\nu_t}{\mathrm{Sc}_t}\frac{\partial \tilde{Y}_k}{\partial x_i} \tag{29}$$

where Sc_t is the turbulent Schmidt number. The dynamic viscosity μ is computed from Sutherland's law. That is,

$$\mu = \mu_0 \left(\frac{T}{T_0} \right)^{3/2} \frac{T_0 + S}{T + S} \tag{30}$$

for a reference viscosity μ_0.

3 NUMERICAL METHODS

In the preceding section, the filtered Navier-Stokes equations are presented along with the equations for LDKM. These equations are well suited for describing turbulent flow fields in any flight regime (subsonic, supersonic and hypersonic). In this part of the report, we discuss the numerical algorithms associated with solving these equations. Our grid generation method is also described. The hypersonic flow problem of interest is characterized by the presence of strong shock waves and high temperature gas dynamics. Historically, it has proven difficult for computer codes to simultaneously capture both shock waves and subtle turbulent flow field fluctuations. This difficulty is caused by differences between high accuracy space schemes and schemes designed to capture strong discontinuities. Generally, numerical dissipation is used to dampen oscillations around shock waves, yet this same dissipation washes away the weaker vortical motions associated with turbulence. On the other hand, high order centered difference stencils are usually required to resolve turbulence eddies, but these stencils cause severe spurious oscillations around shock waves. It is also important to realize that shock-capturing algorithms must be able to contend with complex equations of state. For instance, we prefer to use the thermally perfect gas equation of state in the hypersonic flight regime in order to accurately resolve temperature. To satisfy these requirements, our efforts have produced a two-part scheme. For shock-capturing, we apply what is referred to as the Harten-Lax-van Leer-Contact/Einfeldt (HLLC/E) approximate Riemann solver.[14,15] In smooth regions of the flow field, we apply a second/fourth order MacCormack solver used in the earlier incarnations of LESLIE3D. A switching algorithm allows the computer program to autonomously select the appropriate space scheme based upon local properties throughout the flow field. Below, we present brief descriptions of the spatial integration schemes.

3.1 The HLLC/E Approximate Riemann Solver

HLLC/E is composed of HLLE (HLL-Einfeldt), a scheme that does not preserve the contact wave, and HLLC (HLL-Contact), a scheme that does capture the contact wave. In this context, the contact wave is, in fact, a contact discontinuity, a common flow feature exhibited by the shock tube problem as well as by strong blast waves. These numerical schemes are constructed on a one-dimensional coordinate oriented normal to a finite volume interface. We can orient this coordinate across any of a finite volume cell's interfaces, so the technique is readily usable in three dimensions. The HLLC/E solution is calculated for a vector of conserved variables

$$\vec{U} = (\rho, u, v, w, \rho E, \rho k^{sgs}, \rho Y_1, \ldots, \rho Y_{N_s}) \tag{31}$$

the associated flux vector is

$$\vec{F} = (\rho q, \rho u q + P n_x, \rho v q + P n_y, \rho w q + P n_z, (\rho E + P) q, \rho k^{sgs} q, \rho Y_1 q, \ldots, \rho Y_{N_s} q) \qquad (32)$$

where $q = u n_x + v n_y + w n_z$, and $\hat{n} = n_x \hat{i} + n_y \hat{j} + n_z \hat{k}$ is the unit surface normal vector at the interface.[12] Based upon these definitions, the HLLE numerical flux vector can be written as

$$\vec{F}_{i+1/2}^{HLLE} = \begin{cases} \vec{F}^L, & 0 \le S^L \\ \vec{F}^*, & S^L \le 0 \le S^R \\ \vec{F}^R, & S^R \le 0 \end{cases} \qquad (33)$$

where

$$\vec{F}^* = \frac{S^R \vec{F}^L - S^L \vec{F}^R + S^L S^R (\vec{U}^R - \vec{U}^L)}{S^R - S^L} \qquad (34)$$

One may note from the form of (33), that the HLLE method recognizes a shock discontinuity, but not a contact surface. The Einfeldt wave speed estimates are

$$S^L = \min(q^L - c^L, \breve{q} - \breve{c}) \qquad (35)$$

$$S^R = \max(q^R + c^R, \breve{q} + \breve{c}) \qquad (36)$$

In (35) and (36), c is the speed of sound, and the notation ($\breve{}$) indicates Roe averaging.[16] This numerical flux works quite well for hypersonic flow and is not susceptible to contact instabilities that can occur when strong bow shocks are aligned with the grid. Unfortunately, because of dissipative effects near the contact wave, it cannot be used for extended regions of the flow field where turbulence may be present.[12] It is also best not to apply this scheme for moving shock waves or obliquely oriented shocks. Under these circumstances, the HLLC numerical flux shows improved performance. The numerical flux for the HLLC scheme has a different form, i.e.,

$$\vec{F}_{i+1/2}^{HLLC} = \begin{cases} \vec{F}^L, & 0 \le S^L \\ \vec{F}^{L^*} = \vec{F}^L + S^L (\vec{U}^{L^*} - \vec{U}^L), & S^L \le 0 \le S^* \\ \vec{F}^{R^*} = F^R + S^R (U^{R^*} - U^R), & S^{L^*} \le 0 \le S^R \\ \vec{F}^R, & S^R \le 0 \end{cases} \qquad (37)$$

In (37), intermediate states $\vec{U}^{L^*}$ and $\vec{U}^{R^*}$ are introduced in order to model the presence of the contact discontinuity.[14] These states may be written as

$$\vec{U}^{L^*} = \alpha^L \vec{U}^L + (0, \rho^L \omega^L n_x, \rho^L \omega^L n_y, \rho^L \omega^L n_z, \psi^L, 0, \ldots) \qquad (38)$$

with

$$\beta^L = \frac{S^* - q^L}{S^L - S^*} \tag{39}$$

$$\alpha^L = \beta^L + 1 \tag{40}$$

$$\omega^L = -\beta^L (q^L - S^L) \tag{41}$$

$$\psi^L = \frac{P^* S^* - P^L q^L}{S^L - S^*} \tag{42}$$

and the intermediate wave speed

$$S^* = \frac{P^R - P^L + \rho^L q^L (S^L - q^L) - \rho^R q^R (S^R - q^R)}{\rho^L (S^L - q^L) - \rho^R (S^R - q^R)} \tag{43}$$

The state $\vec{U}^{R*}$ is formed by replacing R for L in (38) through (43). In LESLIE3D, both of these numerical flux formulations are used to form the HLLC/E scheme. We state the result only, i.e.,

$$\vec{F}_{i+1/2}^{HLLC/E} = \begin{cases} \vec{F}_{i+1/2}^{HLLE}, & (d_{P,j} < 0 \text{ and } d_{u,j} < 0) \text{ or } (d_{P,k} < 0 \text{ and } d_{u,k} < 0) \\ \vec{F}_{i+1/2}^{HLLC}, & \text{otherwise} \end{cases} \tag{44}$$

This method requires shock detection in directions transverse to the direction of the interface normal, so

$$d_{P,j} = \frac{|P_{i,j+1,k} - P_{i,j-1,k}|}{\min(P_{i,j+1,k}, P_{i,j-1,k})} - \frac{1}{3} \tag{45}$$

$$d_{u,j} = u_{i,j+1,k} - u_{i,j-1,k} \tag{46}$$

and so forth.

A close inspection of the numerical flux formulas above reveals that the computation of the numerical flux first requires the left (L) and right (R) states be identified at ($i+1/2$), an interface location. These "upwind" states are reconstructed from the data stored in the finite volume cells. This process is accomplished with the use of Monotone Upwind Scheme for Conservation Laws (MUSCL) interpolation.[17] High order interpolation also requires the use of a nonlinear limiter with "flattening" in order to maintain data monotonicity.[18] The details of these procedures are omitted from this work.

3.2 The MacCormack Solver

For the "hybrid" shock-turbulence capturing solver, it is necessary to switch between the upwind scheme and a centralized scheme based upon MacCormack's method when calculating the numerical flux at interfaces. The finite difference version of this scheme uses forward and backward differences alternatively to remove bias from numerical error. For the finite volume scheme, we choose forward and backward upwind variables alternatively for the flux computation, i.e.,

$$\vec{F}_{i+1/2}^{Num} = \vec{F}(\vec{U}_{i+1/2}^{\pm}) \tag{47}$$

where

$$\vec{U}_{i+1/2}^{+} = \vec{U}_{i+1}; \qquad \vec{U}_{i+1/2}^{-} = \vec{U}_{i} \tag{48}$$

It can be shown that this scheme is stable and second order accurate in space. LESLIE3D also offers a MacCormack space scheme accurate to the fourth order. The hybrid method is required to switch back and forth between the upwind and MacCormack solvers. The "switch" is based upon the "smoothness" of the flow field.[19] Principally, LESLIE3D autonomously switches on the upwind scheme only in the vicinity of flow field discontinuities and employs the MacCormack solver in smooth regions of the flow field. This hybrid methodology performs quite well and has been extensively validated for the Richtmyer-Meshkov instability.[19] It has also shown a great deal of efficacy for simulating shock-turbulence interaction problems such as the reactive blast wave.

3.3 Time Integration Scheme and Computer Code Structure

LESLIE3D utilizes explicit time integration to capture the physics associated with unsteady flow fields. Specifically, we find that explicit time integration is very effective for accurately simulating wave propagation. Although, the explicit time step is limited by the Courant-Friedrich-Lewy (CFL) criteria, it presents a high level of efficiency and computational simplicity on parallel machines. A version of the modified Euler method is applied for the MacCormack, upwind and hybrid schemes. This time integration method (in two steps) is briefly summarized for one space dimension as follows.[20]

$$\vec{U}_{i}^{*} = \vec{U}_{i}^{n-1} + \frac{\Delta t}{\Delta x}(\vec{F}_{i+1/2}^{Num,n-1} - \vec{F}_{i-1/2}^{Num,n-1}) \tag{49}$$

$$\vec{U}_{i}^{n} = \frac{1}{2}\left[\vec{U}_{i}^{*} + \vec{U}_{i}^{n-1} - \frac{\Delta t}{\Delta x}(\vec{F}_{i+1/2}^{Num,*} - \vec{F}_{i-1/2}^{Num,*})\right] \tag{50}$$

Equations (49) and (50) require minor adaptations for use with problems cast in three dimensions. Basically, the length term Δx roughly corresponds to a ratio of the cell volume to an average surface area for the interface normal to the coordinate indexed by i. The advective terms

in (2) through (5) are easily discretized for structured, hexahedral finite volumes while the viscous terms require a basic generalized coordinate transformation.[13] The mathematical procedures are relatively easy to accomplish and are quite robust.

3.4 Algebraic Grid Generation

At the beginning of this report, we mentioned that a principal goal of this work is to develop a rapid method of generating grids for a relatively simple body geometry. Our prior work in this area required a great deal of grid generation effort (over 200 blocks). The workload associated with making even the most changes to this grid (such as adding points) is daunting. In this case, we employ a single block grid for a simpler geometry that possesses the desired lobed design. Since the body shown in Figure 1 still possesses some symmetry, the elected plan of attack entails generating a series of two-dimensional grids parallel to the longitudinal body center. These two-dimensional slices can easily be joined laterally to create the three-dimensional mesh. Any of the longitudinal slices can be described by four arcs: one along the body surface, the second along the farfield arc. The third is from the center point on the node to the farfield, and the fourth is from the center point on the tail to the farfield. These arcs are illustrated in Figure 2.

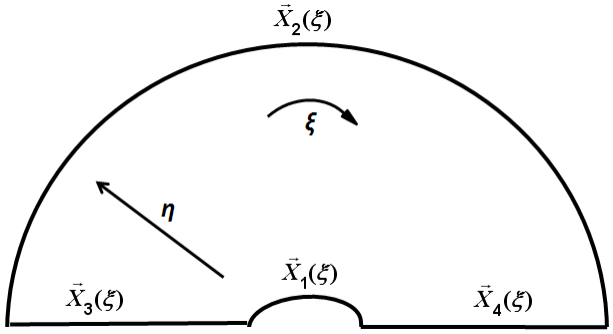

Figure 2. Arrangement of arcs for a two-dimensional grid slice

By establishing a mapping between from arc 1 to arc 2 and then from arc 3 to arc 4, a two-dimensional mesh may be generated. Transfinite Interpolation (TFI) is a commonly applied algebraic technique used to perform this task.[21] TFI is a very fast and easily programmable procedure. Of course, it has its disadvantages. TFI, in its original form, offers little control over point spacing say, adjacent to the body surface. Also, it offers no direct means of enforcing orthogonal intersections of grid lines. One may recall that highly non-orthogonal meshes can result in increased numerical errors in CFD simulations. These errors can be particularly prevalent in the discretization of viscous terms. For this reason, a variant of TFI involving Hermite polynomials is utilized for this work.

In its first incarnation, TFI provides a smooth grid (in many cases) with some control over point spacing. Unfortunately, it offered no control over the slope of grid lines intersecting the boundary. This problem occurred largely because the blending functions employed by TFI allowed only the specification of a point on the boundary.[21] The slope at this point could not be specified. Later on, TFI was improved by incorporating Hermite polynomials as blending functions.[22] These polynomials are more evolved than the older linear blending functions and allow a value for the slope to be specified at the endpoint of an arc. Although offering great

utility, the use of Hermite polynomials does complicate the mapping equations. Referring to Figure 2, we employ the four-boundary method developed by Shih *et al.*[22] We begin by selecting pairs of opposing arcs for the first interpolation step. We select arcs 1 and 2 ("parallel" to the body surface. Let points along arc 1 be denoted as $(X_1(\xi,0), Y_1(\xi,0))$. The first interpolation is conducted in the η direction, so the relevant slopes along arc 1 are designated as

$\frac{\partial X_1(\xi,0)}{\partial \eta}$ and $\frac{\partial Y_1(\xi,0)}{\partial \eta}$. All of these values must be supplied by the user. Accordingly, analogous information must be provided along arc 2, i.e., $X_2(\xi,1)$, $\partial X_2(\xi,1)/\partial \eta$, $Y_2(\xi,1)$ and $\partial Y_2(\xi,1)/\partial \eta$. Let two-dimensional grid points in the field for step 1 be designated as (x^1, y^1); then the step 1 equations are

$$
\begin{aligned}
x^1(\xi,\eta) &= X_1(\xi,\eta)\,h_1(\eta) + X_2(\xi,\eta)\,h_2(\eta) + \frac{\partial x(\xi,\eta=0)}{\partial \eta}\,h_3(\eta) + \frac{\partial x(\xi,\eta=1)}{\partial \eta}\,h_4(\eta) \\
y^1(\xi,\eta) &= Y_1(\xi,\eta)\,h_1(\eta) + Y_2(\xi,\eta)\,h_2(\eta) + \frac{\partial y(\xi,\eta=0)}{\partial \eta}\,h_3(\eta) + \frac{\partial y(\xi,\eta=1)}{\partial \eta}\,h_4(\eta)
\end{aligned}
\tag{51}
$$

Functions h_1 through h_4 are the Hermite polynomials

$$
\begin{aligned}
h_1 &= 2\eta^3 - 3\eta^2 + 1; \quad h_2 = -2\eta^3 + 3\eta^2 \\
h_3 &= \eta^3 - 2\eta^2 + \eta; \quad h_4 = \eta^3 - \eta^2
\end{aligned}
\tag{52}
$$

Equations (51) contains a few strange quantities, the partial derivatives of x and y. These quantities x and y are actually point coordinates for the final grid. What makes these equations strange is that the final grid coordinates are unknown at this stage of the procedure. For the first two or three readings of the core reference, this notation proved to be confusing. What one must realize is that the partial derivatives in (51) are strictly defined along the boundary arcs for the final grid. Yet, these boundary arcs mathematically coincide (up to a discrete distribution of arc points) with arcs (X_1, Y_1) and (X_2, Y_2). Therefore, the notation used in (51) does make sense, and the properties (curvature, etc.) of the curves

$$\vec{X}_1 : \; (x(\xi,\eta=0), y(\xi,\eta=0)) \qquad \text{and} \qquad \vec{X}_2 : \; (x(\xi,\eta=1), y(\xi,\eta=1))$$

are known *a* priori. In fact, these curves provide the opportunity to control the slopes of grid lines along the boundary. We may specify them as follows:

$$\begin{aligned}
\frac{\partial x(\xi,\eta=0)}{\partial \eta} &= -\varphi_1(\xi)\frac{\partial Y_1(\xi)}{\partial \xi}; \quad \frac{\partial y(\xi,\eta=0)}{\partial \eta} = \varphi_1(\xi)\frac{\partial X_1(\xi)}{\partial \xi} \\
\frac{\partial x(\xi,\eta=1)}{\partial \eta} &= -\varphi_2(\xi)\frac{\partial Y_2(\xi)}{\partial \xi}; \quad \frac{\partial y(\xi,\eta=1)}{\partial \eta} = \varphi_2(\xi)\frac{\partial X_2(\xi)}{\partial \xi}
\end{aligned} \tag{53}$$

Functions $\varphi_{1,2}$ are used to control orthogonality of the grid lines and also to help prevent grid adjacent lines from crossing.[23] Notice that the derivatives of *x* (with respect to η) depend upon the derivatives of *y* (with respect to ξ). A similar statement can be made for derivatives of *y*. Note that the right hand sides equation (53) are calculable since point coordinates for arcs 1 and 2 are known. The negative signs shown in (53) are essential in controlling grid line orthogonality at the boundary. More particularly, recall that the normal line slope to a point on an arc is given by the negative reciprocal of arc slope at the point.

Equations (52) and (53) perform an accurate and well controlled interpolation between arcs 1 and 2 in the η direction. However, the resulting distribution of points fails to match arcs 3 and 4. A second interpolation representing the ξ direction is warranted. As is dictated by original TFI theory, the second step interpolates the errors generated by the first step.[21] This dictum is enforced here, but the equations differ slightly from the classic TFI equations. The goal of this step is to determine increments $(\Delta x(\xi,\eta), \Delta y(\xi,\eta))$ such that

$$\begin{aligned}
x(\xi,\eta) &= x^1(\xi,\eta) + \Delta x(\xi,\eta); \\
y(\xi,\eta) &= y^1(\xi,\eta) + \Delta y(\xi,\eta)
\end{aligned} \tag{54}$$

where $(x(\xi,\eta), y(\xi,\eta))$ are the final grid points' coordinates (unless one elects to redistribute points along the grid lines). These increments are calculated as follows.

$$\begin{aligned}
\Delta x(\xi,\eta) &= [X_3(\eta) - x^1(\xi=0,\eta)]\,h_5(\xi) + [X_4(\eta) - x^1(\xi=1,\eta)]\,h_6(\xi) \\
&+ \left(\frac{\partial x(\xi=0,\eta)}{\partial \xi} - \frac{\partial x^1(\xi=0,\eta)}{\partial \xi}\right) h_7(\xi) + \left(\frac{\partial x(\xi=1,\eta)}{\partial \xi} - \frac{\partial x^1(\xi=1,\eta)}{\partial \xi}\right) h_8(\xi)
\end{aligned} \tag{55}$$

$$\begin{aligned}
\Delta y(\xi,\eta) &= [Y_3(\eta) - y^1(\xi=0,\eta)]\,h_5(\xi) + [Y_4(\eta) - y^1(\xi=1,\eta)]\,h_6(\xi) \\
&+ \left(\frac{\partial y(\xi=0,\eta)}{\partial \xi} - \frac{\partial y^1(\xi=0,\eta)}{\partial \xi}\right) h_7(\xi) + \left(\frac{\partial y(\xi=1,\eta)}{\partial \xi} - \frac{\partial y^1(\xi=1,\eta)}{\partial \xi}\right) h_8(\xi)
\end{aligned} \tag{56}$$

where the Hermite polynomials are expressed as

$$\begin{aligned}
h_5 &= 2\xi^3 - 3\xi^2 + 1; \quad h_6 = -2\xi^3 + 3\xi^2; \\
h_7 &= \xi^3 - 2\xi^2 + \xi; \quad h_8 = \xi^3 - \xi^2
\end{aligned} \tag{57}$$

The partial derivatives of *x* and *y* set along the boundary in (56) and (57) are defined below.

$$\frac{\partial x(\xi=0,\eta)}{\partial \xi} = \varphi_3(\eta)\frac{\partial Y_3(\eta)}{\partial \eta}; \quad \frac{\partial y(\xi=0,\eta)}{\partial \xi} = -\varphi_3(\eta)\frac{\partial X_3(\eta)}{\partial \eta}$$
$$\frac{\partial x(\xi=1,\eta)}{\partial \xi} = \varphi_4(\eta)\frac{\partial Y_4(\eta)}{\partial \eta}; \quad \frac{\partial y(\xi=1,\eta)}{\partial \xi} = -\varphi_4(\eta)\frac{\partial X_4(\eta)}{\partial \eta} \tag{58}$$

Equations (55) and (56) also contain derivatives of the stage 1 grid coordinates (x^1, y^1). The formulas for these derivatives are produced by differentiating (51). We simply list the results.

$$\frac{\partial x^1(\xi=0,\eta)}{\partial \xi} = h_1(\eta)\frac{\partial x(\xi=0,\eta=0)}{\partial \xi} + h_2(\eta)\frac{\partial x(\xi=0,\eta=1)}{\partial \xi} + h_3(\eta)\frac{\partial^2 x(\xi=0,\eta=0)}{\partial \xi\,\partial \eta} + h_4(\eta)\frac{\partial^2 x(\xi=0,\eta=1)}{\partial \xi\,\partial \eta} \tag{59}$$

$$\frac{\partial x^1(\xi=1,\eta)}{\partial \xi} = h_1(\eta)\frac{\partial x(\xi=1,\eta=0)}{\partial \xi} + h_2(\eta)\frac{\partial x(\xi=1,\eta=1)}{\partial \xi} + h_3(\eta)\frac{\partial^2 x(\xi=1,\eta=0)}{\partial \xi\,\partial \eta} + h_4(\eta)\frac{\partial^2 x(\xi=1,\eta=1)}{\partial \xi\,\partial \eta} \tag{60}$$

$$\frac{\partial y^1(\xi=0,\eta)}{\partial \xi} = h_1(\eta)\frac{\partial y(\xi=0,\eta=0)}{\partial \xi} + h_2(\eta)\frac{\partial y(\xi=0,\eta=1)}{\partial \xi} + h_3(\eta)\frac{\partial^2 y(\xi=0,\eta=0)}{\partial \xi\,\partial \eta} + h_4(\eta)\frac{\partial^2 y(\xi=0,\eta=1)}{\partial \xi\,\partial \eta} \tag{61}$$

$$\frac{\partial y^1(\xi=1,\eta)}{\partial \xi} = h_1(\eta)\frac{\partial y(\xi=1,\eta=0)}{\partial \xi} + h_2(\eta)\frac{\partial y(\xi=1,\eta=1)}{\partial \xi} + h_3(\eta)\frac{\partial^2 y(\xi=1,\eta=0)}{\partial \xi\,\partial \eta} + h_4(\eta)\frac{\partial^2 y(\xi=1,\eta=1)}{\partial \xi\,\partial \eta} \tag{62}$$

With the use of the equations presented above, a grid is easily produced for a two-dimensional slice. Derivatives along the boundary arcs occurring in (53) and (58) can be either analytically or numerically calculated. Since we are resolving a viscous flow field, maintaining control over the grid point spacing normal to the body is important. For this reason, points along constant ξ grid lines are redistributed after the two-dimensional grid has been generated. We have elected to redistribute the points via hyperbolic sine arc length transformation.[21] Given the prevalence of this transformation in modern grid generation, the details are omitted from this report.

The final step in this process is to create the three-dimensional grid. Two-dimensional slices are generated at each azimuthal station around the circumference of the body. The aerodynamic body has five lobes, so the shapes of any two adjacent slices differ from one another. Common

longitudinal (*i*) and normal (*j*) indices are used to generate these two-dimensional mesh slices, so connecting them through the azimuthal index (*k*) to form hexahedral volumes is not difficult. This method produces an adjustable mesh very quickly and even permits grid lines spacing controls for the mesh interior. Although our mesh is not highly orthogonal, cells adjacent to the body do have nice aspect ratios.

3.5 Computation of Turbulent Statistics

A topic of great interest in the present work is an investigation of turbulent flow near the aerodynamic body surface. Localized regions of elevated subgrid kinetic energy (a primary indicator variable for turbulence) are examined with statistical analysis methods. We consider three such analyses: (i) a velocity correlation matrix, (ii) the probability distribution function for velocity fluctuations and (iii) the spectrum of turbulent kinetic energy. These statistical investigations are not exhaustive, yet they do render insight into properties of the turbulent flow field at high Mach numbers. To perform a more in-depth study, it would also be necessary to analyze the wave number content of turbulent kinetic energy for two-point correlations.[24]

The velocity correlation matrix shows, on the average, how different fluctuating velocity components correlate with one another in time; that is to say, are the fluctuations, existing at point in space, "like" one another in the way they change? To produce the matrix, we rely on the time average defined as

$$\bar{u} = \frac{1}{T}\int_{t_0}^{t_0+T} u(t)\, dt \tag{63}$$

Equation (63) is interesting because, at face value, it seems to remove all time dependency from the time averaged quantity. In fact, this interpretation is used within the context of this report. Still, there is a wider interpretation of (63). Since the time average relies upon parameters t_0 and T, t_0 is the point in time where the average is anchored while T can be thought of as the "width" of the averaging window. The interpretation is more clearly illustrated by rewriting (63) with the transformation $\tilde{t}_0 = t_0 + T/2$, i.e.,

$$\bar{u}(\tilde{t}_0) = \frac{1}{T}\int_{\tilde{t}_0-T/2}^{\tilde{t}_0+T/2} u(t)\, dt \tag{64}$$

Velocity fluctuations are computed as follows. Let u_i denote the i^{th} component of fluid velocity. Then the average of this component is denoted as $\bar{u}_i$, and its associated fluctuation is computed as

$$u_i' = u_i - \bar{u}_i \tag{65}$$

Based upon (63), the velocity (one-point) correlation matrix is defined as

$$\overline{u_i' u_j'} = \overline{u_i u_j} - \bar{u}_i \bar{u}_j \tag{66}$$

where the properties of averaging have been used.[24] Important aspects of turbulent physics are contained in this matrix. For instance, the turbulent kinetic energy per unit mass *E* is closely related to its trace. Observe that

$$E = \tfrac{1}{2}\mathrm{Tr}[\overline{u_i' u_j'}] = \tfrac{1}{2}(\overline{u_1'^2} + \overline{u_2'^2} + \overline{u_2'^2}) \tag{67}$$

Equation (67) is an analogue of the common fluid kinetic energy. The off diagonal matrix entries describe how changes in component velocity fluctuations are related. For example, if $\overline{u_1' u_2'} > 0$, then a positive change in u_1' tends to coincide, on the average, with a positive change in u_2'. On the other hand, $\overline{u_1' u_2'} > 0$, implies the changes must have opposing signs.[25] These correlations may be used to determine, in part, the level homogeneity or isotropicity possessed by turbulent fluctuations.

Since turbulent fluctuations are inherently random, they may be analyzed in accordance with the rules of probability. Velocity fluctuations existing at a point in space are therefore distributed in accordance with a probability distribution function (PDF). Given a random data set, we may estimate the PDF denoted by the letter *f*. The simple method for doing so is by histogram.[26] Suppose that the data consists of a finite number *N* of bounded velocity fluctuations, i.e., there exist finite numbers $u_{i,\min}'$ and $u_{i,\max}'$ such that

$$u_{i,\min}' \le u_i' \le u_{i,\max}' \tag{68}$$

for all *N* samples. Equation (68) delineates a domain in $\Re^3$ that may be divided into a number of bins. Each bin has size $\Delta u_i' = (u_{i,\max}' - u_{i,\min}')/M_i$ where the M_i are the numbers of bins established by the analyst along each coordinate. In this report, we calculate bivariate joint PDFs, e.g., $f(u_i', u_j')$. The mechanics of calculating this PDF begin by setting all (M_i)(M_j) bins to zero. Next we loop over all *N* fluctuations; if a particular pair of fluctuations (u_i', u_j') falls within the a bin delineated by (68), we add the quantity

$$\Delta f = \frac{1}{N(\Delta u_i')(\Delta u_j')} \tag{69}$$

to the bin sum for *f*. Clearly, for samples consisting of small numbers *N* of fluctuations, many bin sums may remain zero, so *f* may be discontinuous. Still, with the use of (68) and (69), the cumulative distribution function (CDF) is properly normalized, i.e.,

$$\lim_{u_i', u_j' \to \infty} F(u_i', u_j') = \int_{-\infty}^{\infty} \int_{-\infty}^{\infty} f(u_i', u_j')\, du_i'\, du_i' = 1 \tag{70}$$

The simple PDF is adequate for studying the behavior of turbulent velocity correlations, but it is not very smooth (especially for small data sets). A smoother PDF may be constructed by dispensing with the idea of bins and summing Gaussian functions for each pair of velocity fluctuations in the data set. As is shown below, this PDF is easily written in the form of an equation.

$$f(u',v') = \sum_{n=1}^{N} \frac{A}{N} \exp\left[-\left\{ \frac{(u'-u'_n)^2}{2\sigma_u^2} + \frac{(v'-v'_n)^2}{2\sigma_v^2} \right\} \right] \tag{71}$$

In (71), (u'_n, v'_n) is a pair of velocity fluctuations taken from the data. The coordinate widths of the Gaussian are taken from the diagonal entries of the velocity correlation matrix (66). Specifically, $\sigma_u = \sqrt{\overline{u'^2}}$, and $\sigma_v = \sqrt{\overline{v'^2}}$. Equation (71) must be normalized to satisfy the requirements of the CDF (70); accordingly, *A* is the normalization constant and can be shown to be

$$A = \frac{1}{2\pi \sigma_u \sigma_v} \tag{72}$$

For this PDF, selection of the domain of integration in (70) is very important. During numerical integration, one must ensure the domain is large enough to ensure that the CDF is computationally normalized.

The final tool addressing turbulent statistics employed in this work is spectral analysis. Turbulent fluid motions are characterized by a wide range of scales, both temporal and spatial. Turbulent eddies have different length and time scales. Spatial scales have a direct spectral analogue known as wave number, and time scales have a similar analogue known as frequency. Both of these analogues lend insight to the structure of turbulence. Here, we address only the time-frequency spectrum of turbulent kinetic energy. In our formulation, turbulent kinetic energy *E* is defined as a function of time at a single point in space, i.e.,

$$E(t) = \tfrac{1}{2}(\overline{u_1'^2(t)} + \overline{u_2'^2(t)} + \overline{u_2'^2(t)}) \tag{73}$$

The frequency spectrum is rendered by Fourier transformation of (67).[24,25] The forward transformation is defined as

$$\hat{E}(\omega) = \frac{1}{2\pi} \int_{-\infty}^{\infty} E(t) \exp(-i\,\omega t)\, dt \tag{74}$$

while the inverse transformation is written

$$E(t) = \int_{-\infty}^{\infty} \hat{E}(\omega) \exp(i\omega t)\, d\omega \tag{75}$$

where ω is angular frequency and "i " is the imaginary unit. Transforms (74) and (75) are "general"; in practice, we do not recognize the concept of negative time or negative frequency, so the lower the limits of the transform integrals are set to zero. The theoretical transforms are also continuously defined unlike the discrete data set addressed later in this report. It follows that we must use the discrete Fourier transform (DFT) in lieu of (74). The DFT is defined for N data points non-uniformly distributed in time as

$$\hat{E}(\omega) = \frac{1}{2\pi} \sum_{n=1}^{N-1} E(t_n) \exp(-i\omega t_n)(t_{n+1} - t_n), \quad \omega \geq 0 \tag{76}$$

$\hat{E}(\omega)$ is a complex function of real ω, so to express the frequency content of E, we plot the power spectral density defined, in this case as

$$P_E(\omega) = \sqrt{\hat{E}(\omega) * \hat{E}(\omega)} \tag{77}$$

a real valued function of ω. DFTs must be used with great care, especially for small data sets due to induced numerical errors such as aliasing. To remedy, in part, this type of difficulty, we observe the limitation imposed by the Nyquist sampling frequency.[27] Noting that $\omega=2\pi f$, where f is regular frequency in Hertz, the Nyquist limitation states that the DFT can resolve no frequencies exceeding f_{Nyq} where

$$f_{Nyq} = \frac{1}{2\Delta t_{\max}} \tag{78}$$

where $\Delta t_{\max}$ is the maximum time step between any two events adjacent in the time series. Obviously, from (78) there is inverse relationship between the time step between data points and the maximum resolvable frequency. Secondly, and not evidenced by (78) are relationships involving the minimal resolvable frequency as well as the ability to resolve two adjacent frequencies. This type of resolution say, the minimum Δf is inversely proportional to the length of time encompassed by the entire time series. Thus, to resolve progressively lower frequencies, we must sample the time series for more time. Moreover, to resolve two different frequencies, we must sample an interval of time that covers at minimum an integer number of complete event cycles for both frequencies. Comparing frequency spectra for turbulent kinetic energy at different space points is a goal of this report.

4 SETTING UP THE SIMULATION

This section of the report describes measures taken to set up the simulation. We endeavor to include enough information to allow others to conduct their own numerical studies on our geometry.

4.1 Grid Geometry

A picture of the body geometry is shown in Figure 1. As mentioned in Section 3.4, the grid is constructed from two-dimensional slices connected in azimuth. The surface of the body is the no-slip surface located at j = 1. The overall body length is 7 cm. The maximum radius of the body (r_{max}) is 1.5 cm while the minimum body radius (r_{min}) is 0.5 cm. The body is characterized by five lobes arranged in azimuth as shown in Figure 3. Because of the lobes, the maximum

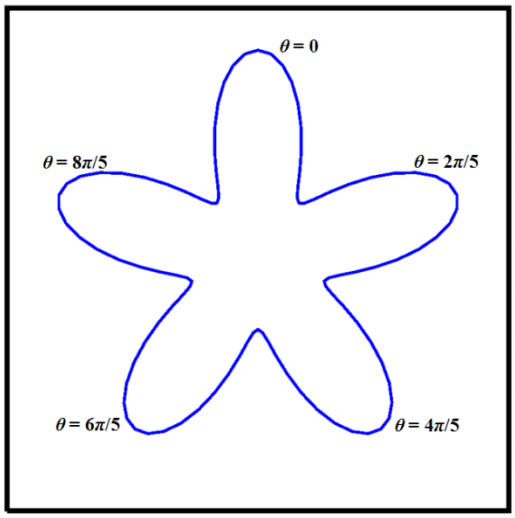

Figure 3. Azimuthal plot of the outer contour of the body illustrating the lobe positions.

inner radius (contour $\vec{X}_1$ in Figure 2) of the two-dimensional slice changes at each azimuthal station. The variation in this radius is dictated by the following equations.

$$\begin{aligned} h &= \bar{h} + \Delta h \cos(5\theta), \quad 0 \le \theta \le 2\pi \\ \bar{h} &= \tfrac{1}{2}(r_{max} + r_{min}) \\ \Delta h &= \tfrac{1}{2}(r_{max} - r_{min}) \end{aligned} \tag{79}$$

The front or nose of each slice is comprised of a disk of fixed radius r_{min}. On the other hand, the rear of each slice is comprised of a disk of radius r_{max} only when $\theta = 2\pi n/5$, $n = 0, 1, \ldots, 4$. In order for the body to terminate at a single point, slices located at other values of θ the rear slice contour is given by the same circular arc (radius r_{max}) multiplied by h. This multiplier has the effect of flattening the circular arc. Figure 4 illustrates the placement of three of the $\vec{X}_1$ slice

contours; note that the vertices for the front and rear arcs are separated by five centimeters. It is evident that arc representing the rear of the body is flattened for those values of θ not coinciding with r_{max}. The final portion of the $\vec{X}_1$ contour is the straight line segment joining the forward and rear arcs. Experience has shown that this line must smoothly intersect (via continuous derivative) the forward and rear arcs in order to achieve a smooth distribution of grid lines.

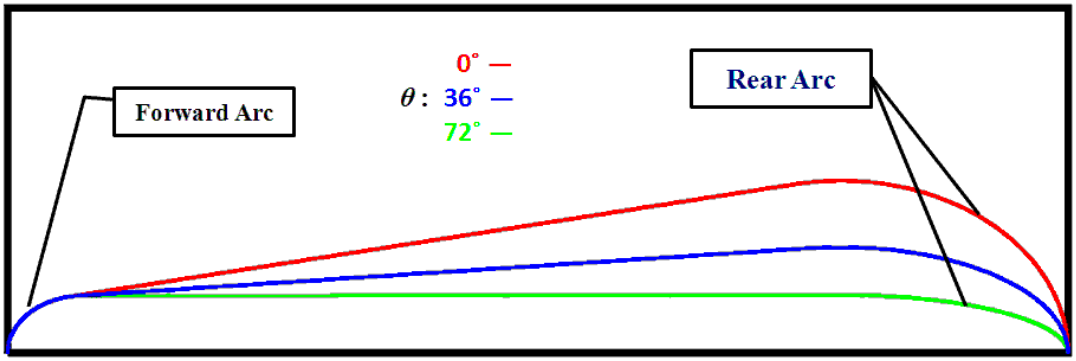

Figure 4. Illustration of body surface contours for different azimuth angles (slices). Each of these contours forms the X_1 contour for generating the grid on the associated azimuthal slice.

Smooth intersections may be accomplished by locating two points, one on the rear side of the forward arc and the other on the forward side of the rear arc, where the derivative taken with respect to the longitudinal coordinate *x* are the same. By including more points along this contour the intersection becomes progressively smoother.

The far field grid contour delineated by points $\vec{X}_2$ in Figure 2 is formed by a simple circular arc with a radius of 15 cm. Contours $\vec{X}_3$ and $\vec{X}_4$ are straight line segments that are common to all slices. Note also that the overall domain has a spherical shape. These four contours are used as inputs by the Hermite TFI routine described in Section 3.4. The grid utilized to generate results for this problem has 301 points in the longitudinal (*i*) direction and 201 points in each of the normal (*j*) and azimuthal (*k*) directions. Minimum spacing at the body surface is set at 10^{-5} meters corresponding to a y^+ value of just under ten.[24]

4.2 Initial Conditions

As mentioned earlier, the aerodynamic body is immersed in a Mach 10 flow field at sea level. The body is oriented at 5˚ pitch and 5˚ yaw. The simulation is started by setting the associated Cartesian velocities for these conditions in the outer spherical shell of farfield cells. In the same cells, subgrid kinetic energy is initialized to a value of 0.01 times the freestream kinetic energy. The freestream temperature is set at 300˚K. Farfield boundary conditions must be specified for LESLIE3D. This process is performed in the initial conditions by checking for the presence of inflow in the outer cell layer. Suppose the $\vec{V}$ is the local velocity and $\hat{n}$ is the outward pointing normal vector for a farfield cell. The boundary condition is then set as

$$\text{Farfield BC} = \begin{cases} \text{Inflow} & \vec{V} \bullet \hat{n} < 0 \\ \text{Outflow} & \vec{V} \bullet \hat{n} > 0 \end{cases} \tag{80}$$

The present computational study uses turbulent mixing and is non-reactive. Since it is non-reactive, only oxygen and nitrogen gases are involved in the problem. This problem is executed on 512 processors (actually cores). The average time step is about 10^{-11} seconds, and 1.383 million time steps are executed. Each step requires about 0.7 seconds of wall clock time. We allow the flow to settle through a travel distance of 11.5 body lengths before collecting data.

5 RESULTS

The lobed body's Mach 6 flight has been simulated as specified in the Section 4. Bulk properties such as pressure, temperature, subgrid kinetic energy and vorticity have been extracted from the numerical solution and used to guide the extraction of statistical information. Time series information is also collected regarding oscillatory forces exerted on the body as well as turbulent velocity fluctuations and kinetic energy.

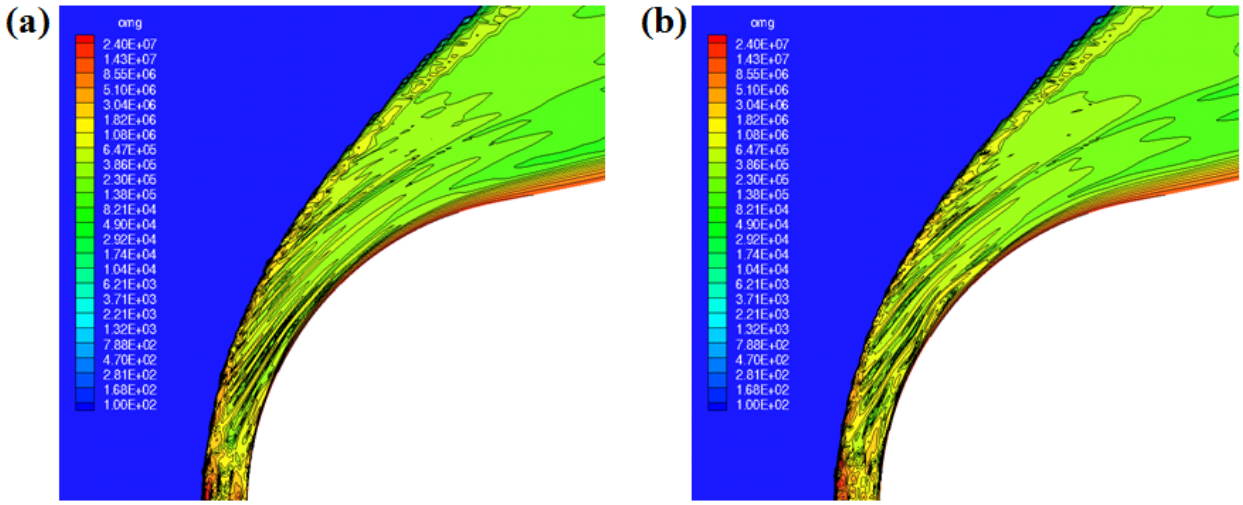

Figure 5. Contour plots of vorticity magnitude set on a vertically oriented plane at the body centerline. Plot (a) occurs at 0.428 ms solution time while plot (b) occurs at 0.439 ms.

5.1 Surface Vorticity

Figure 5 shows two contour plots of vorticity magnitude adjacent to the body's nose The bow shock is clearly visible and has a standoff distance of 0.678 mm from the nose. As is expected, high levels of vorticity are generated behind the curved bow shock and are washed downstream along the body surface. The vorticity field undergoes significant change over the 0.011 ms time interval between these two snapshots. The presence of strong vorticity fluctuations in this region motivates a closer examination of the flow region containing the boundary layer. The same vertical plane in the solution is examined in Figure 6 with enhanced magnification. The mesh is overlain on these plots to provide a means of geometric reference. These plots are interesting

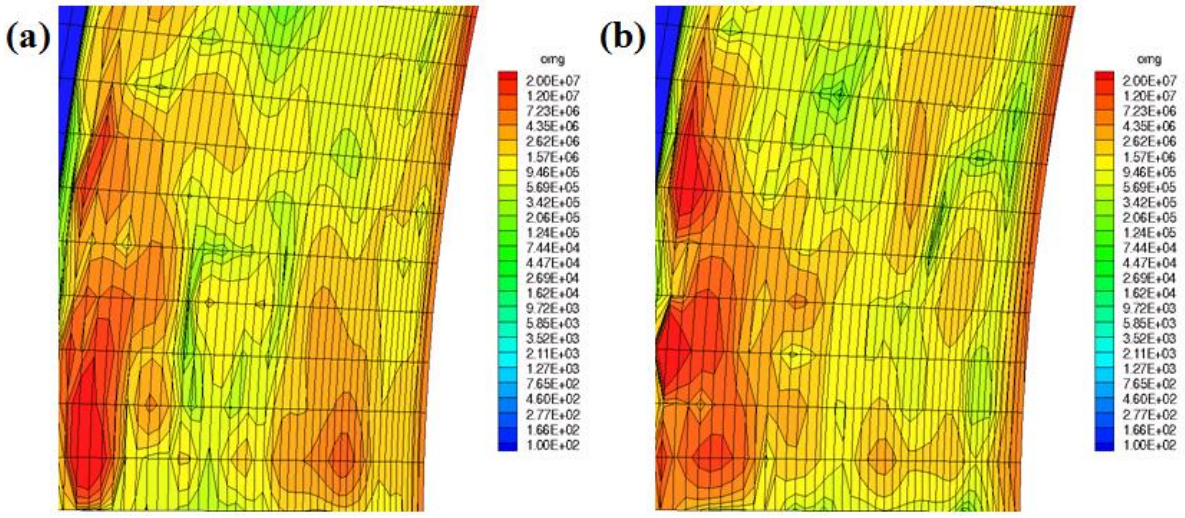

Figure 6. Magnified contour plots of vorticity magnitude showing eddy organization set on a vertically oriented plane at the body centerline. Plot (a) occurs at 0.428 ms solution time while plot (b) occurs at 0.439 ms.

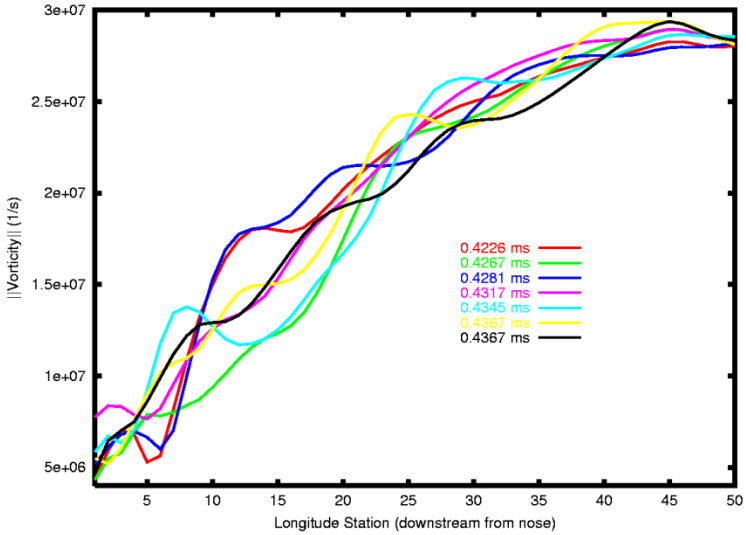

Figure 7. Vorticity magnitude plotted for the body adjacent cell at seven different solution times. The horizontal axis relates the number of grid cells downstream from the node along the body surface.

since we can see vorticity generated at the shock surface (as expected), yet it is even more compelling to observe the flow in the region nearest to the body surface. Without losing too much generality, we can regard the regions inside of closed contours in 6(a) and 6(b) as eddies. Nearest the wall, these eddies seem to propagate upstream (to figure left) and then move downstream along the body. This motion is certainly admissible since the flow behind the curved shock is subsonic. Due to the coupling of vorticity and pressure fluctuations, we expect that a form of feedback exists in this region of the flow, so it becomes worthwhile to assess the strength of vorticity fluctuations in the boundary layer. These fluctuations may drive the production of turbulence. Figure 7 provides an answer to this question albeit over a fairly limited time interval. This figure plots vorticity magnitude in the body adjacent cell over a span of 0.141 ms. Each

curve plots vorticity magnitude at each station along the body surface from the nose. It is evident that boundary layer vorticity is very unsteady in time and drives the production of subgrid kinetic energy through contributions to total strain rate in equation (24). As a result, turbulence is produced in the boundary layer and continues to affect the downstream flow field.

5.2 Surface Pressure and Temperature

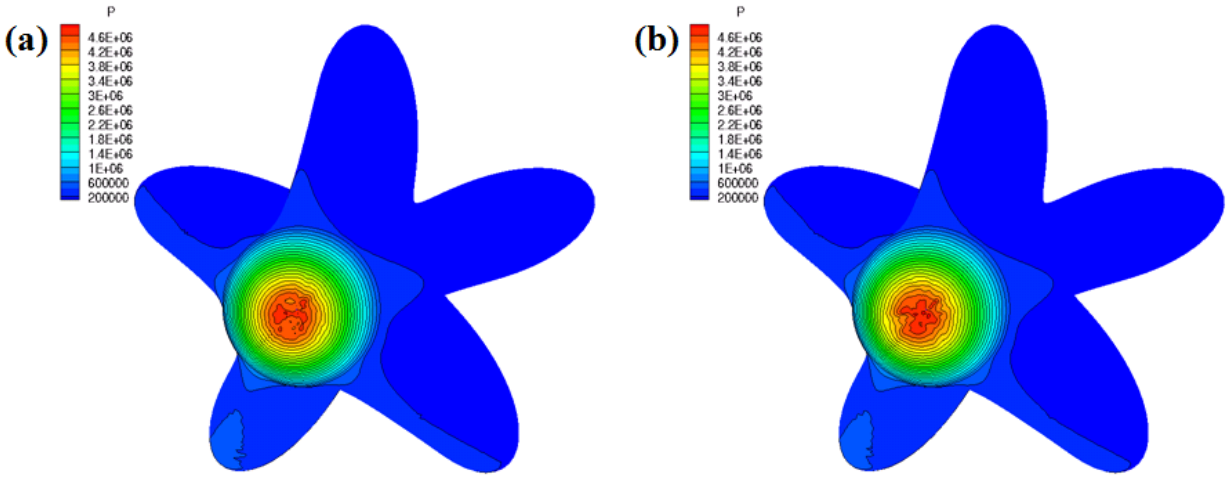

Figure 8. Plots of thermodynamic pressure at the body surface for (a) 0.428 ms and (b) 0.439 ms.

Hypersonic flow fields are characterized by escalating pressure and temperature at the surface of an immersed body. Pressure rises sharply at stagnation points in the flow field while the temperature rise is more widespread as the flow decelerates under the force of skin friction. Figure 8 contains plots of pressure at the body surface at 0.428 ms and 0.439 ms. Given the relatively simple geometric configuration for the body, the pressure field is unremarkable except for pressure fluctuations on the nose. Due the action of turbulent eddies at the surface, pressure contours distort and change periodically in time. This distortion is also noted on the lower left "windward" lobe of the configuration where the oncoming hypersonic flow strikes head on. The numerical solutions show that under time averaging, pressure fluctuations are strongly correlated with fluctuations in the velocity components. Table 1 contains estimates for the pressure-velocity correlations calculated at three points near the tip of the nose.

Table 1. Pressure-Velocity correlation estimates for sampling points at the body surface near the nose tip.

	Top	Leeward	Windward
$< \acute{P}\acute{u} >$	1.71×10^{-4}	9.65×10^{-4}	2.09×10^{-3}
$< \acute{P}\acute{v} >$	3.55×10^{-5}	1.36×10^{-3}	-1.27×10^{-2}
$< \acute{P}\acute{w} >$	3.99×10^{-3}	1.57×10^{-3}	-7.93×10^{-3}

Vertical velocity v shows the strongest correlation with pressure fluctuations at sampling point on the "windward" side of the nose relatively close to the centerline.

For this body configuration, both surface temperature and temperature gradient have been examined. Temperature is of particular interest due to its role in inducing chemical reactions

between oxygen and nitrogen in the surrounding air. Although we have not yet attempted to simulate the attendant chemical reactions, we can determine as to whether or not temperature is high enough to support ionization and dissociation reactions. Body surface temperature based upon the adiabatic wall assumption is shown in Figure 9. These plots suggest that a significant

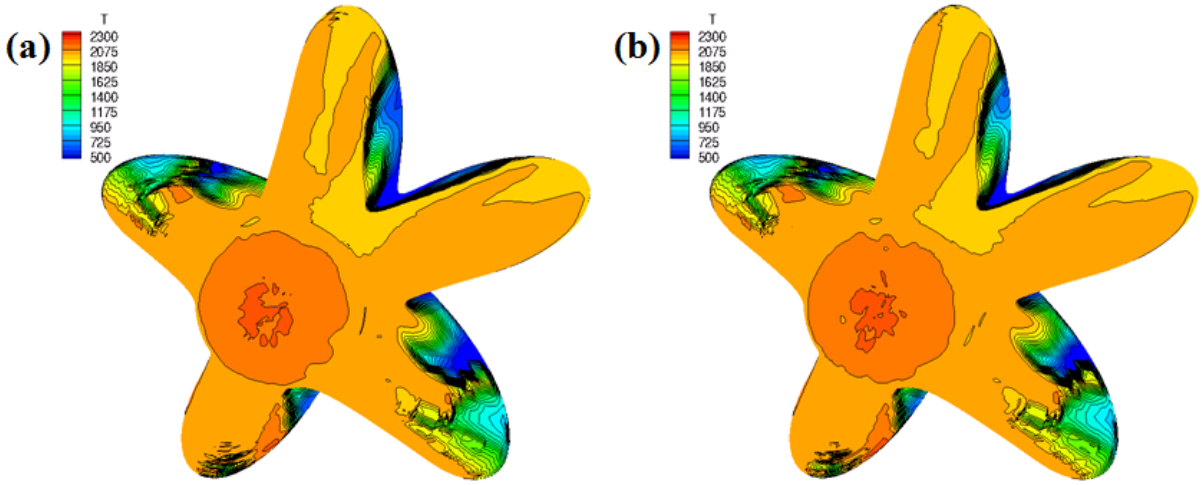

Figure 9. Plots of surface temperature (˚K) based upon the adiabatic wall assumption set at solution times (a) 0.428 ms and (b) 0.439 ms.

temperature gradient exists in the lobed region of the body. We can also see evidence of temperature fluctuations over the body surface (analogous to the pressure fluctuations noted earlier). Figure 10 contains plots of the temperature gradient's magnitude calculated at the body surface. These plots do show extremely high temperature gradients at the body surface particu-

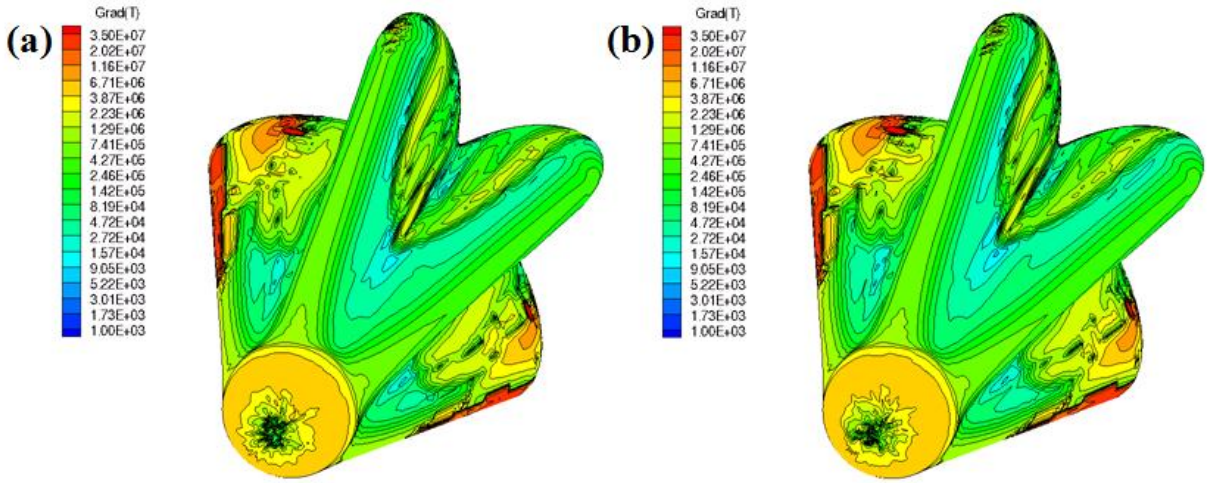

Figure 10. Plots of surface temperature gradient magnitude (˚K/m) based upon the adiabatic wall assumption set at solution times (a) 0.428 ms and (b) 0.439 ms.

larly on the windward lobes and even in the shielded region between the leeward lobes. In the hottest regions, temperatures exceed 2000˚K. As a result, chemical reactions are permissible over a large fraction of the frontal body area.

5.3 Turbulence Statistics

In keeping with previous remarks, a primary focus of this numerical study is to examine the evolution of turbulent flow at hypersonic Mach number for an immersed body of relatively simple construction. For LDKM, subgrid kinetic energy drives the production of subgrid stresses and therefore turbulence. We begin by examining plots of subgrid kinetic energy shown in Figure 11. Two points on the body surface are selected in Region 1 for statistical sampling, and

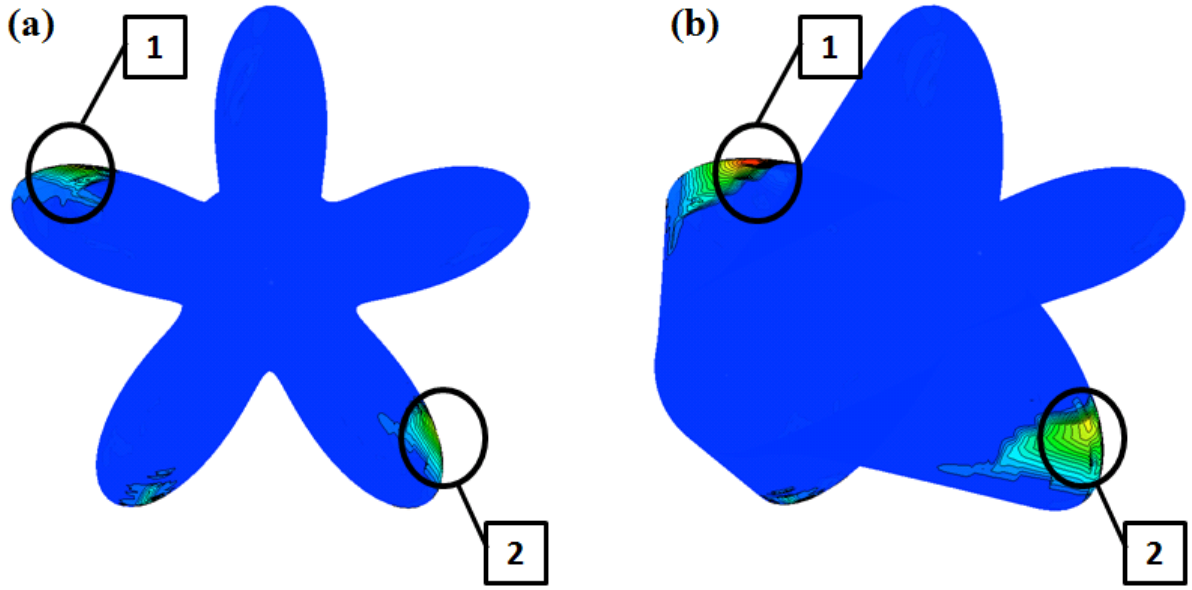

Figure 11. Plots of subgrid kinetic energy on the body surface at 0.428 ms (a) frontal view and (b) oblique view. Points are selected for statistical sampling from region 1 and from region 2 on the lobe surfaces.

likewise, two points are selected in Region 2 where subgrid kinetic energy is substantially elevated. At each sampling point, time series are computed for velocity component fluctuations as well as for turbulent kinetic energy. Velocity correlation matrices are also computed for the velocity fluctuations. In concert with the time series, this information is used to compute probability distribution functions (PDFs) for velocity fluctuations at each sampling point. These PDFs are presented and discussed below.

The first sampling point is chosen at $(i,k) = (200,76)$ in Region 1. Both simple and Gaussian PDFs for the *uv*-correlation have been obtained at this point and are presented in Figure 12. PDFs for the *uw* and *vw* correlations are presented in Figures 13 and 14, respectively. The simple PDF, indicated by (a) in each figure very much resembles a scatter plot formed for the velocity fluctuations and, in itself, allows the analyst to determine the sense of the velocity correlation. On the other hand, the Gaussian PDF serves as better indicator of symmetry or of skewness associated with the distribution function. These three figures are interesting because all of the correlations are positive. An increase (or decrease) in one velocity component tends to indicate a respective increase (or decrease) in the other two velocity components. Also, the PDFs indicate a small skewness in the distributions. The mean is shifted to the "right" in each case. Perhaps due to limitations in the amount of data, the distributions are not fully symmetric. An increase in the

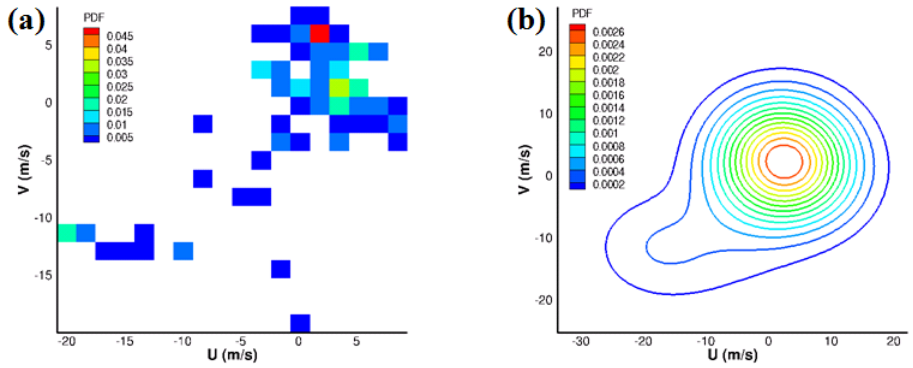

Figure 12. Simple (a) and Gaussian (b) PDFs for the *uv* correlation at Region 1 sampling point (200,76).

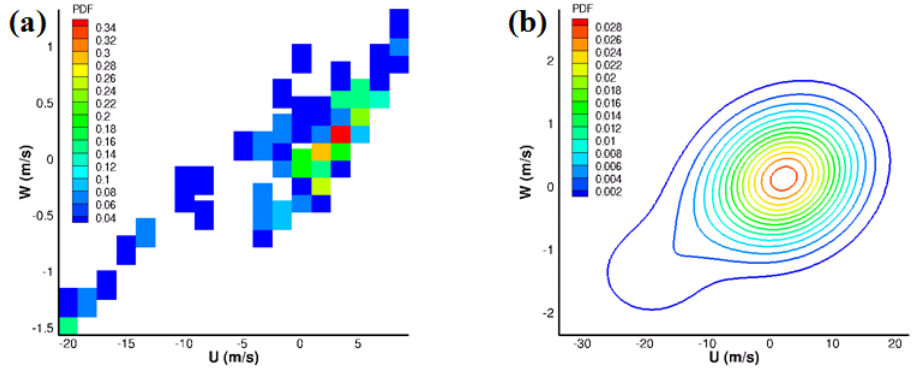

Figure 13. Simple (a) and Gaussian (b) PDFs for the *uw* correlation at Region 1 sampling point (200,76).

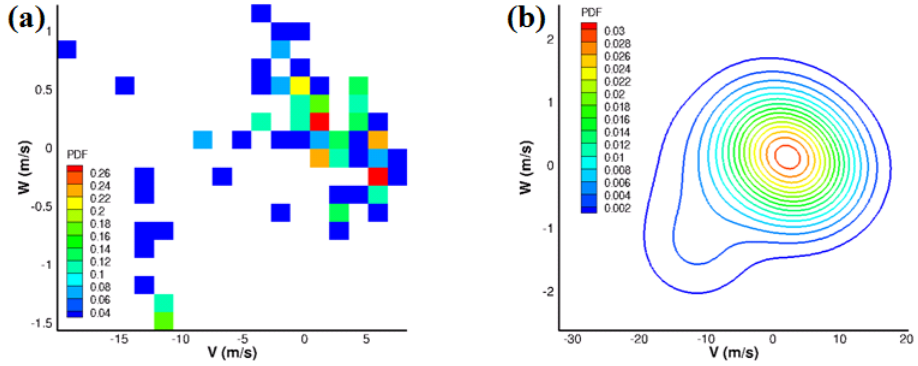

Figure 14. Simple (a) and Gaussian (b) PDFs for the *vw* correlation at Region 1 sampling point (200,76)

length of the time series may change this result.

PDFs for the Region 1 sampling point (*i*,*k*) = (210,75) are provided in Figures 15, 16 and 17. These figures contain PDFs for the *uv*, *uw* and *vw* velocity correlations, respectively. These plots are interesting because, even though the sampling point is geometrically close to (200,76), the *uw* and *vw* correlations are negative. This result is the opposite of that encountered at the neighboring sample point. Secondly, these two correlations exhibit a high level of skewness; their PDFs are noticeably stretched. These results indicate that the eddies with drastically opposite velocity arrangements occur very close together on the body surface.

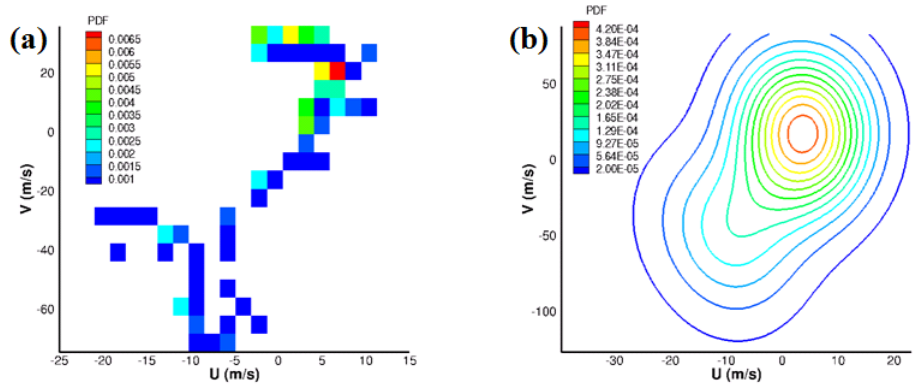

Figure 15. Simple (a) and Gaussian (b) PDFs for the *uv* correlation at Region 1 sampling point (210,75).

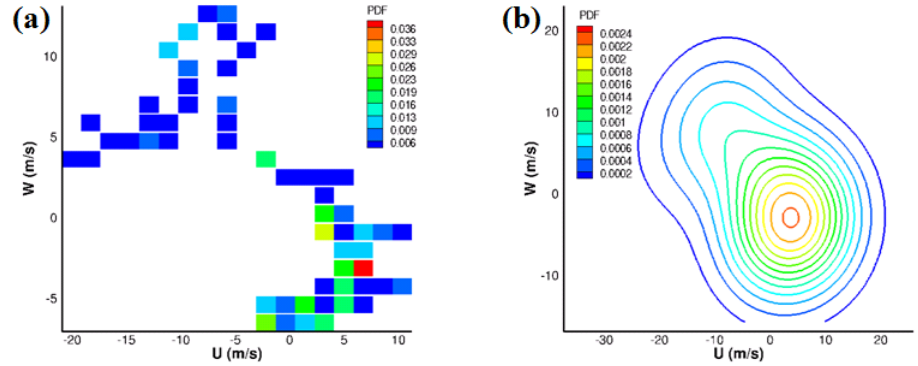

Figure 16. Simple (a) and Gaussian (b) PDFs for the *uw* correlation at Region 1 sampling point (210,75).

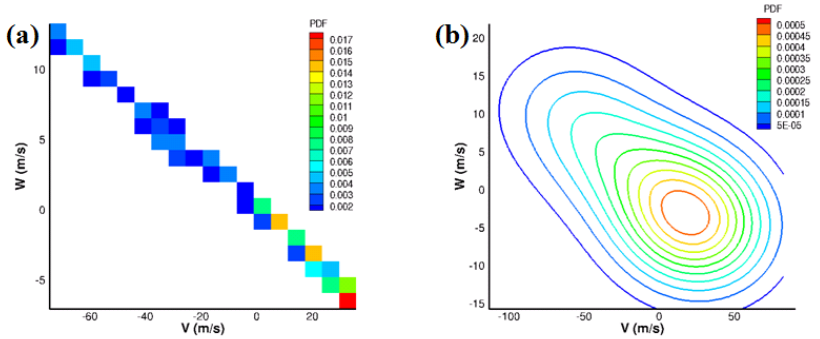

Figure 17. Simple (a) and Gaussian (b) PDFs for the *vw* correlation at Region 1 sampling point (210,75).

In Figures 18, 19 and 20, the velocity correlation PDFs (retaining the same order) are shown for sampling point (*i*,*k*) equal to (215,166). This sampling point resides in Region 2 as indicated in Figure 11. The *uv* and *uw* PDFs shown in Figures 18 and 19 indicate correlated velocity components, but corresponding correlation matrix entries are somewhat low. Still, the *u* and *v* fluctuations are positively correlated at this point. The corresponding simple PDFs show a significant amount of scatter in the solution as evidence of poorer correlation. On the other hand, the *vw* correlation is very positive and clearly reflects the order exhibited by the simple PDF. Each of these PDFs exhibits a skewed distribution tending to favor a decrease-*v* — decrease-*w* tail in the PDF.

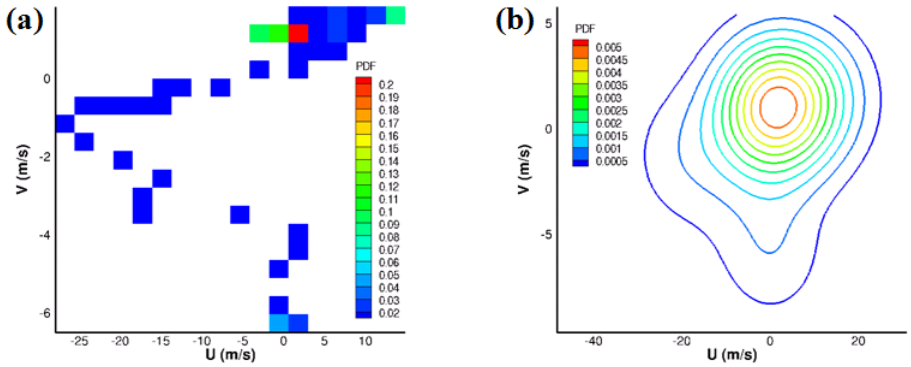

Figure 18. Simple (a) and Gaussian (b) PDFs for the *uv* correlation at Region 2 sampling point (215,166).

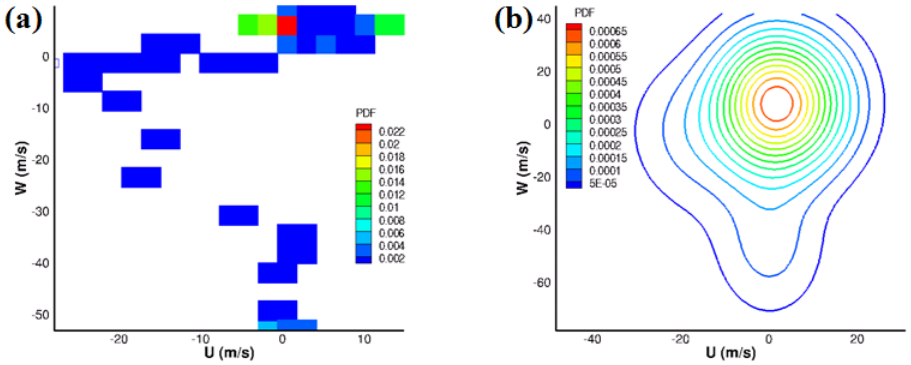

Figure 19. Simple (a) and Gaussian (b) PDFs for the *uw* correlation at Region 2 sampling point (215,166).

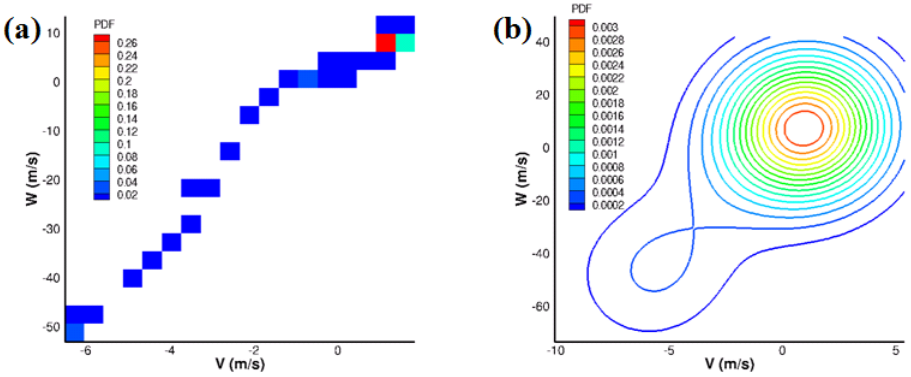

Figure 20. Simple (a) and Gaussian (b) PDFs for the *vw* correlation at Region 2 sampling point (215,166).

In the way of clarification, the PDFs shown in the figures in this section of the report are graphed in terms of equi-probability contours. This statement applies to both the simple and Gaussian PDFs. Figures 21,23 and 23 exhibit the PDFs for sampling point (*i*,*k*) set at (230,168), a point in relatively close proximity to the preceding point (215,166) also in Region 2. One can see that the *v* velocity fluctuations correlate negatively with the corresponding *u* and *w* components while the *u* and *w* positively correlate. It is also evident that the correlation matrix components are quite large representing large covariance values. The resulting PDFs are spread widely over the velocity planes and have reduced point magnitudes. Each of these PDFs is skewed with a significant tail leading away from the mean. Yet, there is less scatter among the fluctuating velocity components. Some of the skewness may be due to the small sample size

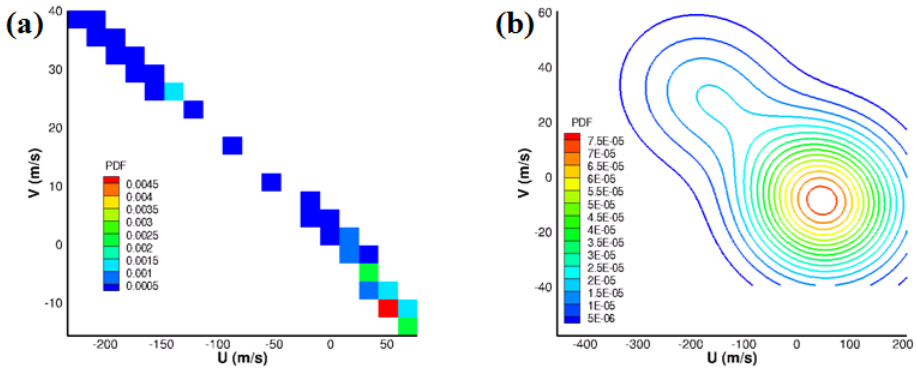

Figure 21. Simple (a) and Gaussian (b) PDFs for the *uv* correlation at Region 2 sampling point (230,168).

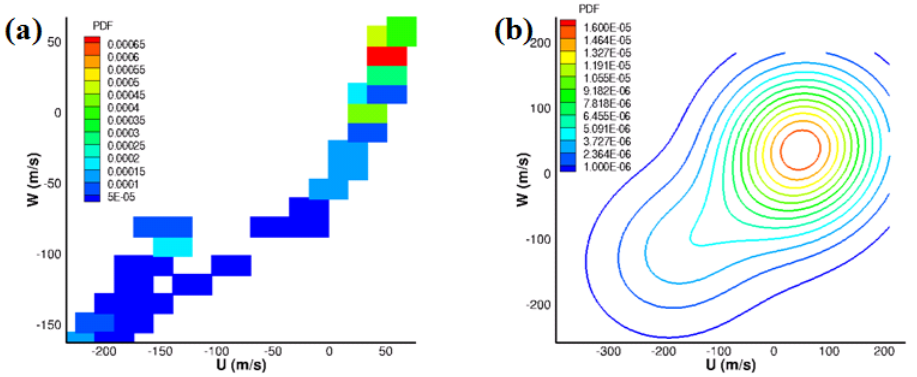

Figure 22. Simple (a) and Gaussian (b) PDFs for the *uw* correlation at Region 2 sampling point (230,168).

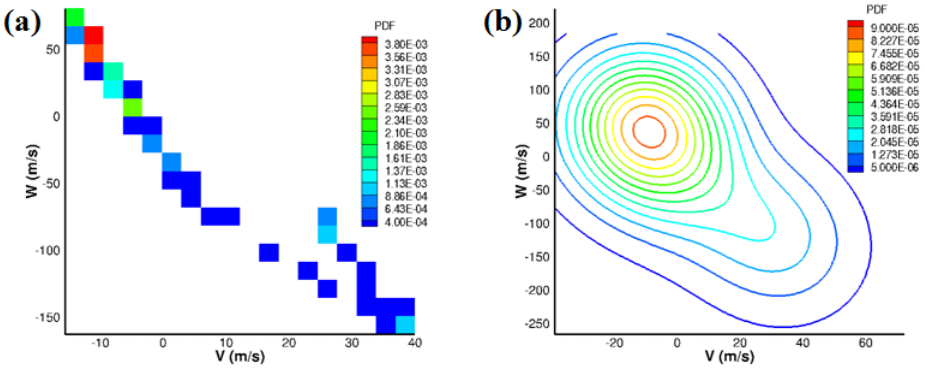

Figure 23. Simple (a) and Gaussian (b) PDFs for the *vw* correlation at Region 2 sampling point (230,168).

used for this analysis. Overall, it is interesting to see how different the covariance matrix entries are for two closely spaced points in the same region. Examples are the *uw* correlations for Region 1 and both the *uv* and *vw* correlations calculated in Region 2. At each sampling point, the velocity fluctuations exhibit randomness albeit with components with widely differing magnitudes in certain cases. The covariance matrix entries illustrate this concept quite well and prove very useful in computing the Gaussian-based PDF.

5.4 Turbulence Spectra

Turbulence involves a wide range of scales in fluid motion as energy cascades from the scales of the mean (exterior) flow field down to the smallest scales where fluid kinetic energy is dissipated in the form of heat.[24] Thus far, we have conveyed no direct information that indicates the scale(s) associated with velocity fluctuations. In this section, we provide evidence of the scales involved through the inclusion of time-based spectra. Here we examine spectra for velocity component fluctuations and of turbulent kinetic energy (67). Power spectral densities are calculated via discrete Fourier transformation (Section 3.5) to convey the frequency content of fluctuating quantities. The spectra are calculated at the same sampling points used in the preceding section. Consider sampling point (i,k) = (200,76); its power spectral density is provided in Figure 24. Although the spectrum is inactive for frequencies below 200,000 rad/s,

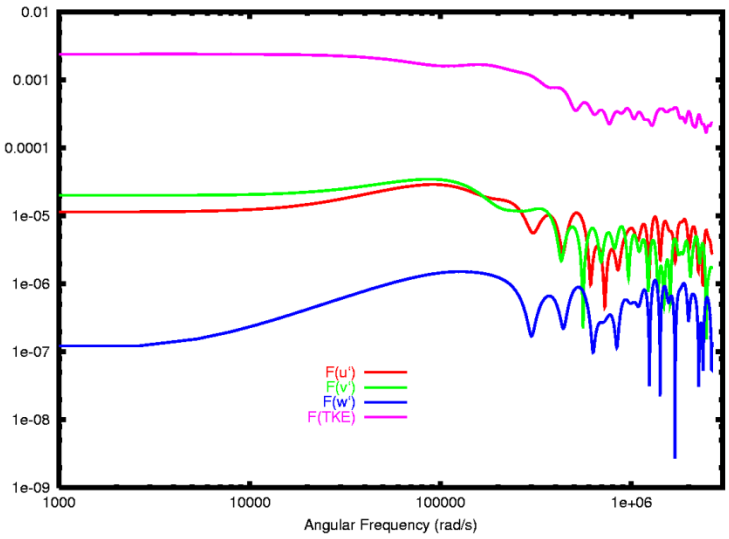

Figure 24. Power spectral densities for all three fluctuating velocity components and for turbulent kinetic energy calculated at sampling point (200,76) in Region 1.

but there is a great deal of activity in the high frequency section. In its entirety, the spectrum shown occurs below the Nyquist frequency. The lack of activity in the low frequency section is likely due to the short sampling interval of 0.049 ms. A significant increase in the sampling interval is needed not only to capture lower frequency eddies but also to sharpen or better resolve the high frequency peaks in the spectrum. Figure 24 is clear evidence of a great deal of small scale motion. This behavior is also reflected at sampling point (210,75). Its spectrum, again computed in Region 1, is shown in Figure 25. The notation F($\acute{u}$), F($\acute{v}$), F($\acute{w}$) and F(TKE) represents the power spectral densities for the three fluctuating velocity components and for turbulent kinetic energy, respectively. Although this spectrum also has low activity at lower frequencies, the high frequency bands are even more energetic. This behavior is quite noteworthy because the two sampling points in question are in close proximity to one another. For further information, we consider sampling points in Region 2. The spectra for sampling point (215,166) are presented in Figure 26. Again, the high frequency segment of the spectrum is very active, but the low frequency segment is not developed well due to the short sampling interval. The smooth curves in this section are not characteristic of fully developed spectra. A jagged spectrum is expected in the low frequency range, but a greatly expanded sampling interval is

needed in order to obtain it. Similar spectral behavior is exhibited in Figure 27, computed for sampling point (230,168) in Region 2.

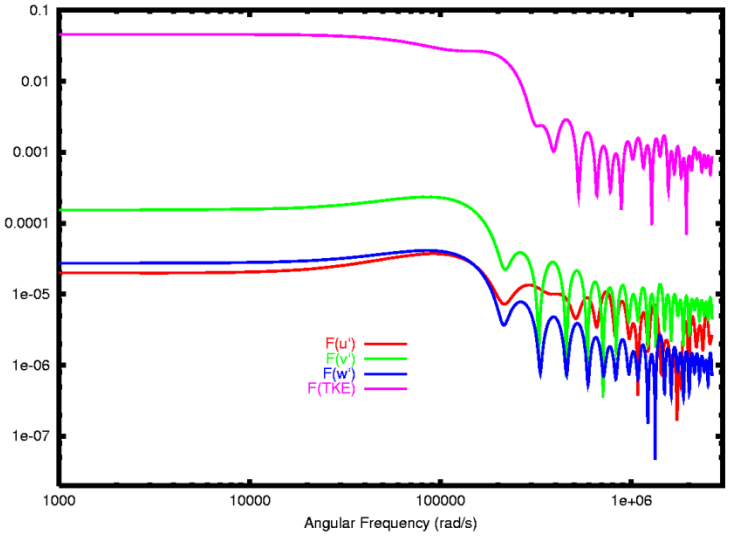

Figure 25. Power spectral densities for all three fluctuating velocity components and for turbulent kinetic energy calculated at sampling point (210,75) in Region 1.

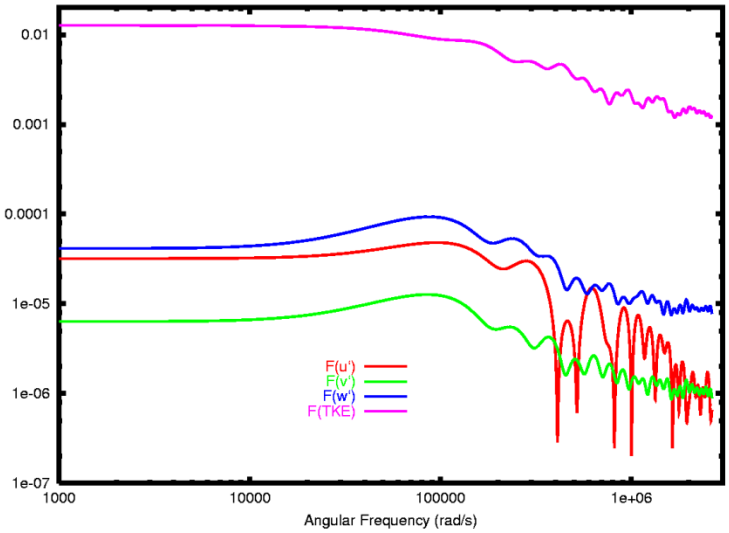

Figure 26. Power spectral densities for all three fluctuating velocity components and for turbulent kinetic energy calculated at sampling point (215,166) in Region 2.

5.5 Aerodynamic Forces

From LESLIE3D's numerical solutions, we have computed the aerodynamic force components F_x, F_y and F_z exerted on the immersed body. This information is also amenable to time series analysis; in particular, frequencies of oscillation can be extracted from the force time history. The turbulent, viscous flow field has a pronounced effect on the aerodynamics of the body since tractions (skin friction) and separated flow (at higher pitch/yaw angles) can strongly alter the forces exerted on the body. The time history for F_x is shown in Figure 28. This plot

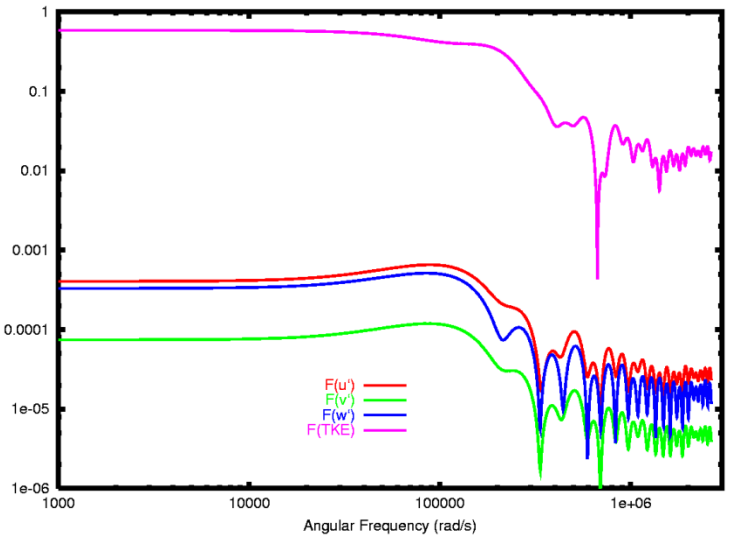

Figure 27. Power spectral densities for all three fluctuating velocity components and for turbulent kinetic energy calculated at sampling point (230,168) in Region 2.

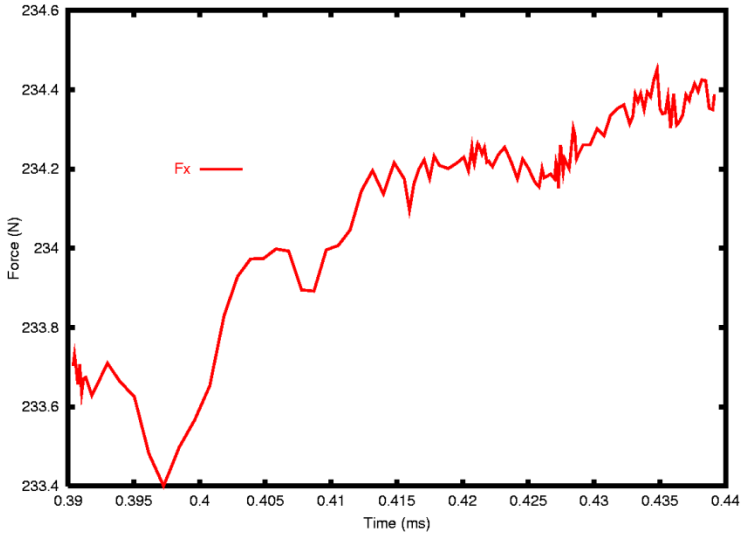

Figure 28. Time history plot of the *x*-component F_x of aerodynamic force exerted on the body.

a great deal of high frequency activity. Yet, there is evidence of some low frequency activity that may not be fully resolved in the relatively small sampling window applied here. Some flow separation, not yet revealed, may cause larger excursions in F_x due to vortex shedding. Plots of the time histories F_y and F_z are shown in Figure 29. In the *y* and *z* directions, the force excursions are not as large as in the *x* direction, but the high frequency content is still present. A low frequency oscillation may also be present. As before, our sampling interval is too short to fully reveal this dynamic. Power spectral densities have been extracted from the force component time histories. Plots of frequency content for these force components are shown in Figure 30. In spite of the small sampling window, the discrete Fourier transformation does resolve some frequency content. A fundamental frequency of oscillation is revealed at 82,000 rad/s. A number of higher frequency peaks are also captured and not necessarily at integer multiples of the fundamental. For instance, a secondary peak is located at 235,000 rad/s and a third at 389,000 rad/s. The high

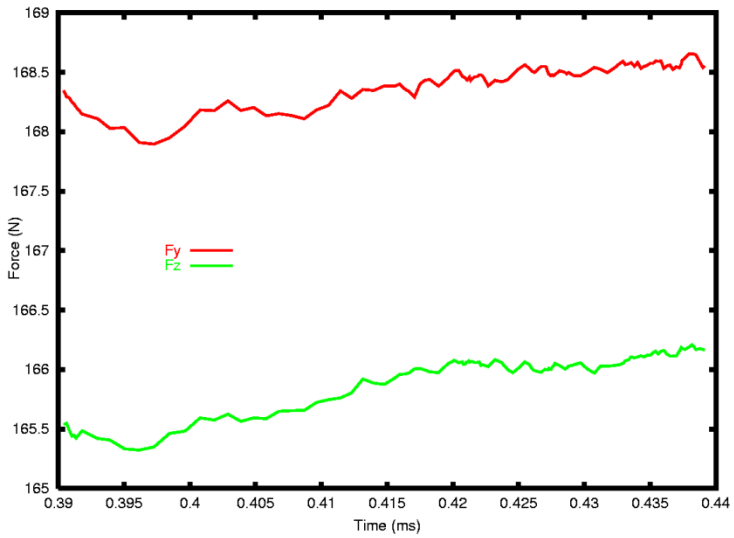

Figure 29. Time history plots of the *x* and *y*-components F_x and F_y of aerodynamic force exerted on the body.

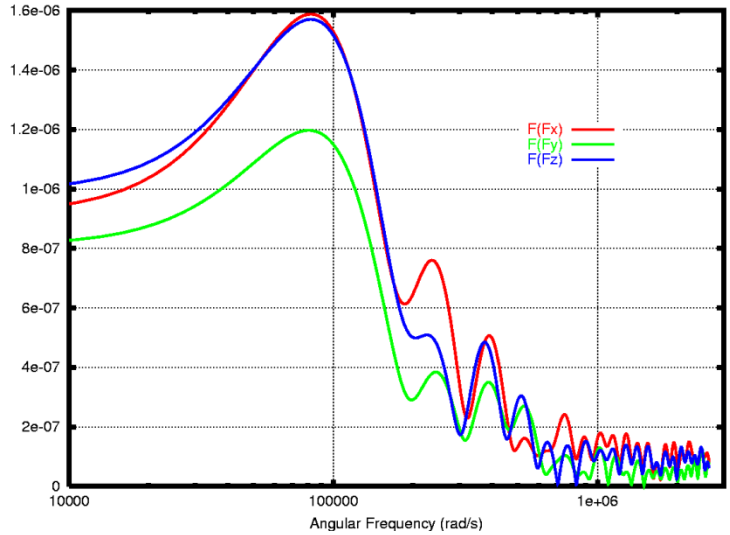

Figure 30. Power spectral density plots for the three aerodynamic force components.

frequency section of the spectrum is very active for all three components indicating the presence of many oscillatory frequency all below the Nyquist sampling frequency. This information stands as a reasonable indicator for the presence of a turbulent flow around the body.

6 CONCLUSIONS

This report has addressed some aspects of the hypersonic aerodynamics of lobed body. In particular, we are concerned with evolution of turbulent flow around the body with a distribution of subgrid kinetic energy defined at the far field boundary of the computational domain. The simulation is conducted at Mach 6, sea level flight conditions, with pitch and yaw angles fixed at five degrees. LESLIE3D, a multiphase physics computer code developed by Suresh Menon at Georgia Tech, is used to perform the simulation on 512 processors. The algorithms employed by

LESLIE3D include the locally dynamic subgrid kinetic energy model with fixed coefficients. A number of results are shown in this report such as body surface pressure, temperature and subgrid kinetic energy. The standoff distance for the curved bow shock has also been included, and a study of vorticity evolution behind the shock and in the boundary layer is discussed. Statistics for the turbulent flow field have been calculated, namely, the velocity covariance matrix. Probability distribution functions have been computed for velocity component fluctuations and turbulent kinetic energy. Time-based spectra are also provided for the same quantities. Aerodynamic force time histories are also provided, and the attendant frequency content has been computed.

The flow field is characterized by turbulent eddies, particularly in regions on the lobes where subgrid kinetic energy is very high. The time sampling interval of 0.049 ms is rather short, so the spectra are not fully developed, particularly at lower frequencies. That is to say, to resolve a frequency of 100 rad/s, a sampling time on the order of 1.6 ms is required. Clearly, more simulation time is required to resolve frequencies this low. Still, the velocity field contains a great deal of random character, and the high frequency spectral band is very active. Fluctuating quantities like velocities, pressure and aerodynamic force demonstrate a high degree of randomness as expected for a turbulent flow field. This behavior is reflected in the results of spectral analyses performed on the velocity field and aerodynamic force components. Each spectrum, although limited by a relatively short sampling window, is characterized by the presence of many high frequency components all captured below the Nyquist frequency. Further spectral study of this flow field is warranted for a substantially wider sampling window.

REFERENCES

1. Génin, F., Fryxell, B. and Menon, S., "Simulation of Detonation Propagation in Turbulent Gas-Solid Reactive Mixtures", *41st AIAA/ASME/SAE/ASEE Joint Propulsion Conference & Exhibit*, Tucson, Arizona, 2005.

2. Génin, F. and Menon, S., "Simulation of Turbulent Mixing Behind a Strut Injector in Supersonic Flow", *47th AIAA Aerospace Sciences Meeting*, Orlando, Florida, 2009.

3. Menon, S., "Direct and Large-Eddy Simulations of Solid Propellant Combustion and High-Energetic Detonation in Reactive Mixtures", Annual Report for Grant N00014-01-1-0951, Office of Naval Research, 2007.

4. Ukai, S., Genin, F., Srinivasan, S. and Menon, S., "Large Eddy Simulation of Re-shocked Richtmyer-Meshkov Instability", *47th AIAA Aerospace Sciences Meeting*, Orlando, Florida, 2009.

5. Balakrishnan, K. and Menon, S., "On the role of ambient reactive particles in the mixing and afterburn behind explosive blast waves", *Combustion Science and Technology*, Vol. 182, No. 2, 2010, pp. 186-214.

6. Anderson, J.D., Jr., *Hypersonic Flow and High Temperature Gas Dynamics*. MacGraw-Hill, Inc., New York, 1989.

7. Hankey, W.L., *Re-Entry Aerodynamics*. AIAA Education Series, American Institute of Aeronautics and Astronautics, Washington, DC, 1988.

8. Vincenti, W.G. and Kruger, C.H., *Introduction to Physical Gas Dynamics*, Krieger Publishing Co., Malabar, FL, 1975.

9. Sankaran, V. and Menon, S., "LES of spray combustion in swirling flows", *Journal of Turbulence,* Vol. 3, No. 1, 11, 2002.

10. Erlebacher, G., Hussaini, M.Y., Speziale, C.G. and Zang, T.A., "Toward the large-eddy simulation of compressible turbulent flows", *Journal of Fluid Mechanics*, Vol. 238, 1992, pp. 155-185.

11. Yeung, P.K., Pope, S.B. and Sawford, B.L., "Reynolds number dependence of Lagrangian statistics in large numerical simulations of isotropic turbulence", *Journal of Turbulence*, Vol. 7, No. 58, 2006, pp. 1-12.

12. Génin, F., "Study of Compressible Turbulent Flows in Supersonic Environment by Large Eddy Simulation", Ph.D. Dissertation, School of Aerospace Engineering, Georgia Institute of Technology, Atlanta, Georgia, May 2009.

13. Warsi, Z.U.A., *Fluid Dynamics: Theoretical and Computational Approaches*, CRC Press, Boca Raton, FL, 1993.

14. Toro, E.F., *Riemann Solvers and Numerical Methods for Fluid Dynamics – A Practical Introduction*. Addison-Wesley Publishing, Co., Inc., 1999.

15. Einfeldt, B., Munz, C.D., Roe, P.L. and Sjogreen, B., "On Godunov-type methods near low densities", *Journal of Computational Physics*, Vol. 92, 1991, pp. 273-295.

16. Roe, P.L., "Approximate Riemann solvers, parameter vectors and difference schemes", *J. Computational Physics*, Vol. 43, 1981, pp. 357-372.

17. Hirsch, C., *Numerical Computation of Internal and External Flow, Volume 2*. John Wiley & Sons, Inc., New York, 1991.

18. Collela, P. and Woodward, P., "The piecewise-parabolic method for hydrodynamics", *Journal of Computational Physics,* Vol. 54, 1984, pp. 174-201.

19. Fryxell, B. and Menon, S., "Hybrid Simulations of Richtmyer-Meshkov Instability", *43rd Aerospace Sciences Meeting and Exhibit*, Reno, Nevada, January 2005.

20. Burden, R.L., Faires, J.D. and Reynolds, A.C., *Numerical Analysis*, 2nd Ed., Prindle, Weber & Schmidt, Boston, MA, 1981.

21. Thompson, J.F., Warsi, Z.U.A. and Mastin, C.W., *Numerical Grid Generation: Foundations and Applications*, Elsevier Science Publishing Co., Maryland Heights, MO, 1985.

22. Shih, T.J.-P., Bailey, R.T., Nguyen, H.L. and Roelke, R.J., "Algebraic grid generation for complex geometries", *International Journal for Numerical Methods in Fluids*, Vol. 13, 1991, pp. 1-31.

23. Liou, Y.C. and Jeng, Y.N., "A transfinite interpolation method of grid generation based upon multipoints", *Journal of Scientific Computing*, Vol. 13, No. 1, 1998, pp. 105-114.

24. Pope, S.B., *Turbulent Flows*, Cambridge University Press, Cambridge, 2000.

25. Tennekes, H. and Lumley, J.L., *A First Course in Turbulence*, MIT Press, Cambridge, MA, 1992.

26. Pope, S.B., "A rational method for determining probability distributions in turbulent reacting flows", *Journal of Non-equilibrium Thermodynamics*, Vol. 4, 1979, pp. 309-320.

27. Hardin, J.C., *Introduction to Time Series Analysis*, NASA-RP-1145, Langley Research Center, 1986.

DISTRIBUTION LIST
AFRL-RW-EG-TR-2013-031

Defense Technical Information Center Attn: Acquisition (OCA) 8725 John J. Kingman Road, Ste 0944 Ft Belvoir, VA 22060-6218	1 Electronic Copy (1 file, 1 format)

EGLIN AFB OFFICES:

AFRL/RWOC (STINFO Tech Library Copy)	1 Copy
AFRL/RW CA-N	Notice of publication only